UCSF
UC San Francisco Previously Published Works

Title

Dodecamer assembly of a metazoan AAA+ chaperone couples substrate extraction to refolding

Permalink

https://escholarship.org/uc/item/571947sn

Journal

Science Advances, 9(19)

ISSN

2375-2548

Authors

Gupta, Arpit
Lentzsch, Alfred M
Siegel, Alex
et al.

Publication Date

2023-05-10

DOI

10.1126/sciadv.adf5336

Copyright Information

This work is made available under the terms of a Creative Commons Attribution-NonCommercial License, available at https://creativecommons.org/licenses/by-nc/4.0/

Peer reviewed

eScholarship.org Powered by the California Digital Library
University of California

BIOCHEMISTRY

Dodecamer assembly of a metazoan AAA+ chaperone couples substrate extraction to refolding

Arpit Gupta[1]†, Alfred M. Lentzsch[1]†, Alex Siegel[1]†, Zanlin Yu[2]‡, Un Seng Chio[2], Yifan Cheng[2,3], Shu-ou Shan[1]*

Copyright © 2023 The Authors, some rights reserved; exclusive licensee American Association for the Advancement of Science. No claim to original U.S. Government Works. Distributed under a Creative Commons Attribution NonCommercial License 4.0 (CC BY-NC).

Ring-forming AAA+ chaperones solubilize protein aggregates and protect organisms from proteostatic stress. In metazoans, the AAA+ chaperone Skd3 in the mitochondrial intermembrane space (IMS) is critical for human health and efficiently refolds aggregated proteins, but its underlying mechanism is poorly understood. Here, we show that Skd3 harbors both disaggregase and protein refolding activities enabled by distinct assembly states. High-resolution structures of Skd3 hexamers in distinct conformations capture ratchet-like motions that mediate substrate extraction. Unlike previously described disaggregases, Skd3 hexamers further assemble into dodecameric cages in which solubilized substrate proteins can attain near-native states. Skd3 mutants defective in dodecamer assembly retain disaggregase activity but are impaired in client refolding, linking the disaggregase and refolding activities to the hexameric and dodecameric states of Skd3, respectively. We suggest that Skd3 is a combined disaggregase and foldase, and this property is particularly suited to meet the complex proteostatic demands in the mitochondrial IMS.

INTRODUCTION

Protein homeostasis is essential for the survival and proper functioning of cells and requires the correct folding, localization, and quality control of most of the proteome (*1*). Misfolding and aggregation of proteins, especially under stress conditions, deprive cells of functional proteins and generate toxic species that lead to a variety of protein misfolding diseases (*2*). To overcome this problem, cells evolved a diverse set of molecular chaperones that participate in every aspect of protein folding and quality control. For example, heat shock protein 70/40 (Hsp70/40) act as central hubs that interact with numerous newly synthesized proteins in the cell (*3*). Hsp70s protect unfolded or partially unfolded proteins from aggregation and, via cochaperone [e.g., Hsp40 (*4*) and nucleotide exchange factors (*5*)]–regulated adenosine triphosphatase (ATPase) cycles, can release client proteins in a conformation conducive to folding (*6*, *7*). Chaperonins, such as the bacterial GroEL and eukaryotic TRiC/CCT complexes, form two stacked seven- to nine-membered rings that encapsulate unfolded polypeptides in a central cavity, which provide a protected environment to facilitate client folding (*8*–*10*). In addition, small Hsps act as "holdases" by binding non-native states of proteins at early stages of misfolding, thus preventing the accumulation of irreversible protein aggregates (*11*). Together, the diverse activities of the different chaperone systems provide a robust network that maintains homeostasis of the proteome.

A special class of molecular chaperones, represented by ClpB in bacteria and Hsp104/Hsp78 in yeast, can further extract proteins from their aggregates and rescue folding (*12*, *13*). These "disaggregases" are members of the ATPases associated with diverse cellular activities (AAA+) family, which assemble into hexameric rings via their nucleotide-binding domains (NBDs) and use ATPase cycles to power the generation of mechanical force. Each NBD extends a pore loop to contact the client protein via a conserved aromatic residue (*14*). Together, the pore loops form a constricted central pore in the NBD ring through which client proteins are threaded in an unfolded conformation, and this threading activity provides the fundamental mechanism by which ClpB/Hsp104 extract substrates from the aggregate (*15*–*17*). Extensive structural work on protein-threading AAA+ members showed that the pore rings form a spiral staircase surrounding the substrate protein, and that the NBD rings adopt varying degrees of spiral distortion linked to the nucleotide state of individual ATPase sites [reviewed in (*18*)]. These works support a sequential mechanism of substrate translocation in which individual NBD protomers progress around the ring and dissociate from the neighboring subunit at the bottom of the spiral upon adenosine triphosphate (ATP) hydrolysis and nucleotide dissociation, and reassociate with the protomer at the top position upon binding ATP; these coordinated movements propel stepwise substrate translocation (*18*–*20*). ClpB/Hsp104/Hsp78 belong to type II AAA+ ATPases that contain two NBD rings working in alternating cycles, with the second NBD (NBD2) serving as the main ATPase motor during substrate translocation. Last, the ability of ClpB/Hsp104/Hsp78 to solubilize and refold aggregated proteins relies on coordination with the Hsp40/70 chaperones (*15*, *21*), which recruit these AAA+ chaperones to protein aggregates, allosterically activate the NBD, and assist in the folding of client proteins after they are released from the AAA+ disaggregase (*22*, *23*).

AAA+-powered disaggregase systems are essential for protecting bacterial and yeast cells from extensive proteotoxic stress. Curiously, at the evolutionary transition to metazoans, ClpB/Hsp104/Hsp78 were lost (*24*), raising puzzling questions about whether and how higher eukaryotic organisms "repair" aggregated proteins. Notably, a partial homolog of ClpB/Hsp104, Skd3, is present in

[1]Division of Chemistry and Chemical Engineering, California Institute of Technology, Pasadena, CA 91125, USA. [2]Department of Biochemistry and Biophysics, University of California at San Francisco, San Francisco, CA 94158, USA. [3]Howard Hughes Medical Institute, University of California at San Francisco, San Francisco, CA 94158, USA.
*Corresponding author. Email: sshan@caltech.edu
†These authors contributed equally to this work.
‡Present address: Cryo-EM Core Facility, BG NIHBC 35A - PNRC II RM 3F-103, 35A Convent Dr., Bethesda, MD 20892, USA.

the intermembrane space (IMS) of mitochondria in multiple metazoan lineages (*25*–*28*). Skd3 knockout leads to the aggregation of a variety of mitochondrial proteins and impairs the innate immune response in cell culture studies (*27*, *29*). In vivo, Skd3 is ubiquitously expressed but has particularly high expression levels in adult brain tissue (*30*). A variety of mutations in Skd3 are linked to a severe mitochondria disorder, 3-methylglutaconic aciduria (3-MGCA), an autosomal recessive disorder with clinical features that include cataracts, neurological disorder, intellectual disability, and severe congenital neutropenia that can develop into leukemia (*30*–*35*).

The mitochondrial IMS is a complex proteostatic environment where a variety of protein biogenesis events occur (*36*, *37*). Mitochondrial inner membrane proteins and matrix proteins need to be maintained in a largely unfolded, translocation-competent conformation while also protected from aggregation as they transit through the IMS. On the other hand, proteins or domains that reside in the IMS need to undergo folding, assembly, and maturation. The small volume of the IMS further renders the local concentration of proteins very high and thus prone to aggregation. However, little is known about protein folding in the mitochondrial IMS. With the exception of the Mia40/Erv system, which catalyzes oxidative protein folding, and the small translocases of the inner membrane (TIM) proteins, specialized for the import of TIM subunits and carriers, no homologs of Hsp40/70/60 have been identified in the mitochondrial IMS. Although it has been suggested that AAA^+ proteases in the mitochondrial IMS contribute to protein folding, this hypothesis is based mainly on observations with protease-deficient mutants. The discovery of Skd3 raises the possibility that it may serve as one of the missing general chaperones in the mitochondrial IMS.

Despite its importance in physiology and pathology, the precise roles and mechanisms of Skd3 are poorly understood. Molecularly, Skd3 is a unique fusion of an AAA^+ ATPase domain, which shares homology with NBD2 of ClpB/Hsp104 (*24*), to an N-terminal ankyrin repeat domain (ARD), a repeat protein scaffold that participates in diverse protein-protein interactions (Fig. 1A). Newly synthesized Skd3 also contains an N-terminal mitochondrial targeting sequence (MTS) that directs its import into mitochondria, where it is sequentially processed by the MPP and PARL proteases (Fig. 1A) (*26*, *27*). Cupo and Shorter (*27*) showed that Skd3 is strongly activated upon PARL-mediated cleavage and that $_{PARL}$Skd3 is a highly potent, stand-alone chaperone. In the absence of additional chaperones, $_{PARL}$Skd3 reactivates aggregated luciferase with efficiencies higher than that of the Hsp104/70/40 system and even solubilizes amyloid fibril formed by α-synuclein, whose aggregation is linked to Parkinson's. Multiple disease-linked mutations in the NBD and ARD of Skd3 impair the reactivation of luciferase aggregates, linking defects in the chaperone activity of Skd3 to pathology (*27*, *38*). Recent cryo–electron microscopy (cryo-EM) structures of an Skd3 hexamer revealed that the NBD of Skd3 forms a hexameric spiral in which multiple pore loop residues from each protomer grip the substrate polypeptide, suggesting that it uses a substrate translocation mechanism conserved among AAA^+ disaggregases (*38*, *39*). However, the molecular mechanism underlying Skd3's effective chaperone activity is poorly understood. Most previous work described Skd3 as a disaggregase akin to ClpB and Hsp104, but how a client protein is efficiently refolded by Skd3 in the absence of additional chaperones is unexplained. Lastly, multiple recent studies reported unusual higher-order assembly of Skd3, showing that Skd3 hexamers can further form dodecamers via contacts between the ARDs (*25*, *26*, *38*, *39*). The roles of the unusual assembly states of Skd3 remain elusive.

In this work, we address these questions using a combination of structural and biochemical studies. We obtained two cryo-EM structures of substrate-bound $_{PARL}$Skd3 hexamers in "open" and "closed" spiral conformations, which capture the disaggregase at different stages of substrate translocation. Akin to the observation from other laboratories, $_{PARL}$Skd3 also forms a cylindrical cage–shaped dodecamer that harbors a large internal cavity. Biochemical studies show that solubilized luciferase is protected by $_{PARL}$Skd3 until it reaches a conformation committed to folding, contrary to expectations for the threading mechanism that describes ClpB/Hsp104. Mutations in the ARD that disrupt the dodecamer interface specifically impair client refolding, suggesting that disaggregation and refolding can be attributed, respectively, to the hexamers and dodecamers of Skd3. Last, the ARD can directly mediate substrate interactions. On the basis of these data, we suggest a working model for how Skd3 couples disaggregation to client refolding to provide an effective repair mechanism for misfolded proteins.

RESULTS

To obtain chaperone-active $_{PARL}$Skd3, we expressed it as a C-terminal fusion to His_6-SUMO. After affinity purification of the fusion protein, cleavage using the SUMO protease Ulp1 generates $_{PARL}$Skd3 containing a defined, native N terminus, which was further purified by size exclusion chromatography to >95% purity (fig. S1A).

To assess the oligomerization of $_{PARL}$Skd3, we used mass photometry, which provides an accurate measurement of the mass of individual molecules and complexes in solution (*40*). As mass photometry operates at submicromolar protein concentrations, we used $_{PARL}$Skd3 bearing a mutation in the Walker B (WB) motif (E455Q) to facilitate detection of Skd3 oligomers, as this mutation reduces ATP hydrolysis rates and thus enhances hexamer assembly. $_{PARL}$Skd3_WB is primarily distributed between three species with measured molecular masses consistent with monomer, hexamer, and dodecamer (Fig. 1B). The population of Skd3 hexamer relative to the monomer is increased by higher Skd3 concentration (Fig. 1B) and by conditions that reduce ATP hydrolysis, including the WB mutation, the slowly hydrolyzing ATP analog ATPγS, and the nonhydrolyzable ATP analog AMPPNP (fig. S1, B to E), confirming that $_{PARL}$Skd3 hexamer assembly is strongly dependent on high ATP occupancy. On the other hand, dodecamers were observed under all conditions that support substantial hexamer formation, suggesting that they are formed by dimerization of hexamers (Fig. 1B and fig. S1, B to E).

Single-particle cryo-EM analysis confirmed the presence of higher oligomeric states in $_{PARL}$Skd3 (Fig. 1C), as reported previously (*25*, *38*, *39*). Top views of the two-dimensional (2D) class averages of $_{PARL}$Skd3_WB bound to ATPγS showed exclusively hexameric rings (Fig. 1C). In side views, particles containing two or three "rings" were observed, and the latter is consistent with the assembly of two hexamers sandwiching the ARD (Fig. 1C). In addition to hexameric rings, wild-type $_{PARL}$Skd3 in ATPγS also formed heptameric rings that can further assemble into higher-order structures (fig. S1F), as was observed in other studies (*38*, *39*). Because the significance of Skd3 heptamer is unclear and

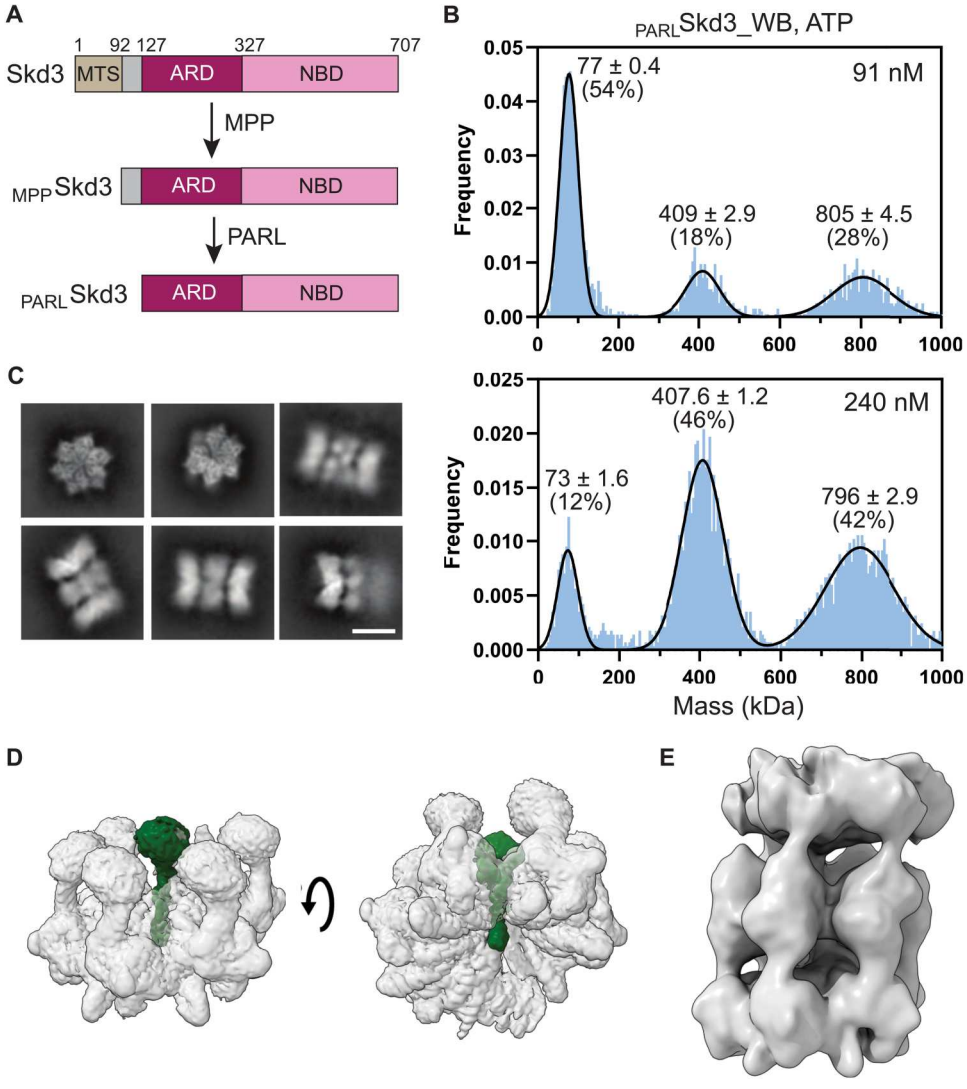

Fig. 1. $_{PARL}$Skd3 assembles into both hexamer and dodecamer. (**A**) Scheme depicting the domain composition of Skd3 and its sequential proteolytic processing in mitochondria. (**B**) Mass photometry measurements of the oligomeric state of $_{PARL}$Skd3_WB at different concentrations in the presence of 2 mM ATP. Gaussian fits of the data (black lines) yield the indicated population of particles in each assembly state. The measured masses of the three populations are indicated and consistent with the predicted molecular weight of $_{PARL}$Skd3 monomer (66 kDa), hexamer (396 kDa), and dodecamer (792 kDa). (**C**) Representative top and side views of cryo-EM 2D class averages of ATPγS-bound $_{PARL}$Skd3_WB. Scale bar, 100 Å. (**D**) Low pass–filtered cryo-EM maps of the Skd3 hexamer. Green highlights the EM density for the bound substrate. (**E**) Cryo-EM map of the Skd3 dodecamer.

because the assembly of $_{PARL}$Skd3_WB is more robust and homogeneous compared to $_{PARL}$Skd3, we carried out the subsequent data collection and structural analyses with $_{PARL}$Skd3_WB assembled in ATPγS. Particle classification (fig. S2) allowed the reconstruction of both the hexamer complex (Figs. 1D and 2), which we describe first, and the dodecamer complex (Figs. 1E and 3), which is described later.

$_{PARL}$Skd3 hexamer structures reveal ratchet-like movements implicated in substrate translocation

$_{PARL}$Skd3_WB hexamer was reconstructed to an overall resolution of 2.77 Å (Fig. 2A, fig. S3, and Table 1). Local resolution ranged from ~2.5 Å in the core of the NBD ring to 3 to 7 Å in the peripheral regions, the P1 protomer, and the ARDs, probably due to conformational flexibility in regions of low resolution (fig. S3A). Except for solvent-exposed loops (524 to 536 and 655 to 675), main-chain atoms could be traced throughout the NBDs starting at residue 318, and side-chain densities were resolved for most residues in the final sharpened map of the NBD hexamer (Fig. 2A and fig. S3G). This allowed us to build an atomic model of the hexamer (Fig. 2B) by rigid-body docking of an AlphaFold-predicted model (*41*) followed by iterative cycles of manual adjustment in COOT (*42*) and real-space refinement in Phenix (*43*). The P1 protomer contains regions with lower resolution than the remainder of the NBD hexamer (fig. S3A) and was therefore modeled on the basis of rigid-body docking of the model for the P4 protomer. The individual NBDs follow the canonical D2 domain structure of ClpB and Hsp104, with a large and a small subunit that cradle ATP.

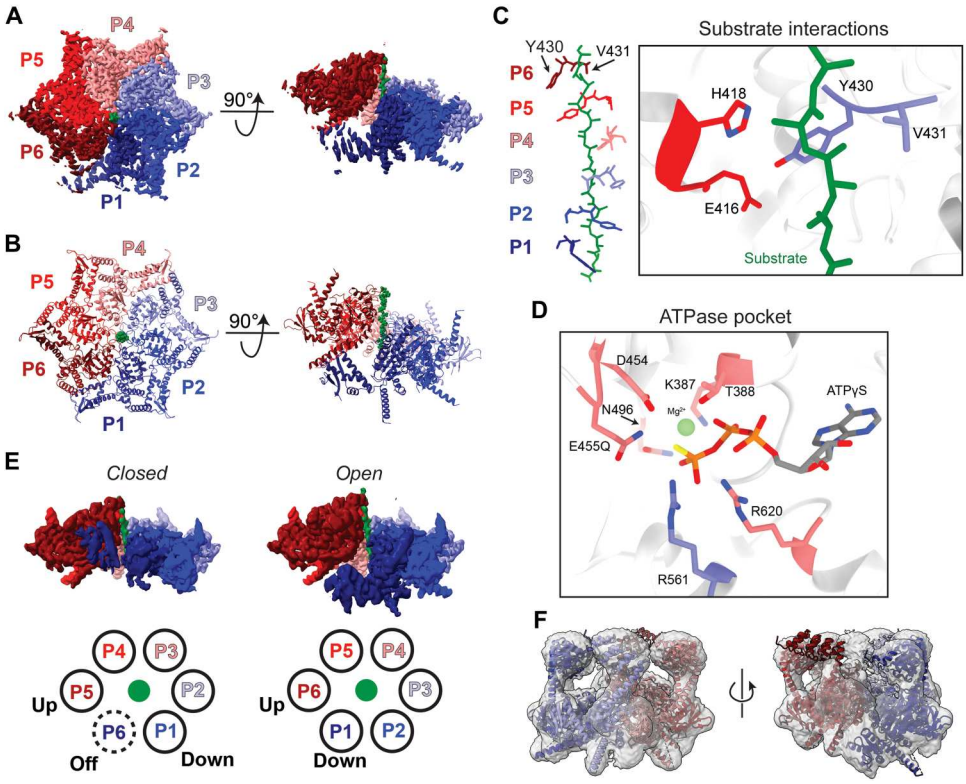

Fig. 2. Cryo-EM structures of substrate-bound $_{PARL}$Skd3 hexamers. (**A** and **B**) Top (left) and side (right) of the high-resolution sharpened EM density map (A) and molecular model (B) for the Skd3 NBD ring. The bound substrate is in green. (**C**) Left, overview of the arrangement of the pore loops surrounding the bound substrate in the open spiral conformation of the Skd3 NBD. Right, zoom in of the contacts of the pore 1 and pore 2 loops with substrate and with one another. (**D**) Active site interaction of the bound ATP in the P4 protomer. (**E**) Comparison of the 3DVA-derived EM density maps for the closed and open spiral conformations of the Skd3 NBD. A lower threshold for the EM density was used to visualize the flexible P6 protomer in the closed conformation. Color coding and the position of the individual protomers are indicated in the scheme below. (**F**) The Skd3 ARD and the interdomain linker were fit as a rigid body to the non-NBD EM density in the low-pass filtered density map of the $_{PARL}$Skd3 hexamer.

Compared to ClpB, Skd3 has a 14–amino acid insertion in the D10 helix that protrudes sideways into solvent, followed by an extended loop (residues 522 to 534) that connects D10 to D11 (fig. S4A). The structures of the individual Skd3 protomers superimpose with a root mean square deviation (RMSD) of <0.6 Å, except for a ~20° inward bend of the interdomain helix in the P6 protomer (fig. S4A).

The NBD ring in most Skd3 hexamers adopts a right-handed open spiral conformation, with P1 to P6 designating the protomers from the lowest to the uppermost positions in the spiral. The pore rings of all six protomers are well resolved and contact an additional contiguous elongated density in the central pore (Figs. 1D and 2A), which was interpreted to arise from a trapped substrate polypeptide and modeled as a poly-alanine chain in the extended conformation. Each protomer contacts the substrate via multiple interactions (Fig. 2, B and C). The conserved Y430 and V431 in the pore loop form the main contacts that clamp the substrate. Analogous to ClpB and Hsp104, Skd3 has a secondary pore loop with multiple residues (E416 and H418) positioned near the substrate polypeptide, although not as close as the primary pore loop (Fig. 2C, right). E416 and H418 are positioned such that they may form interprotomer contacts with the clockwise neighbor. Compared to the Skd3 hexamer structure from Cupo *et al.* (*38*), the Skd3 spiral in the current structure is more extended (Fig. 2B), allowing the pore loop contacts of the six protomers to descend along a total of 12 amino acids in the substrate polypeptide in a steep spiral staircase, each spanning two amino acids (5.5 Å) and completing a 60° turn (Fig. 2C, left).

The resolution of the NBD structure allowed us to assign the nucleotide states of the individual ATPase sites based on the density for the bound ATPγS and the position of key catalytic residues. The Skd3 ATPase site consists of the canonical Walker A motif (K387 and T388), WB motif (D454 and E455), sensor 1 (N496), sensor 2 (R620), the catalytic arginine finger R561, and a network of hydrophobic residues contacting the adenine moiety (Fig. 2D). The catalytic side chains are well resolved in protomers P2 to P5 and less well resolved in P1 and P6, suggesting higher flexibility in these seam protomers (fig. S4C). Protomers 2 to 6 show well-resolved density for ATPγS, which coordinates a Mg^{2+} via the nonbridging oxygens on the β- and γ-phosphates (Fig. 2D and fig. S4C). In addition, the arginine finger R561 from the clockwise neighboring protomer was positioned near the γ-phosphate in P2 to P6, a hallmark of the catalytically active conformation. In the P1 protomer, in contrast, weaker and partial density was observed for ATPγS, and the catalytic contact from R561 is missing (fig. S4C). Thus, protomers P2 to P6 are ATP-bound in the open spiral of Skd3, whereas P1 is likely in a mixture of post-hydrolysis and apo states.

The structure rationalizes many disease-linked mutations in Skd3 (fig. S5). Residues R408, E435, Y617, R628, and E639 lie on

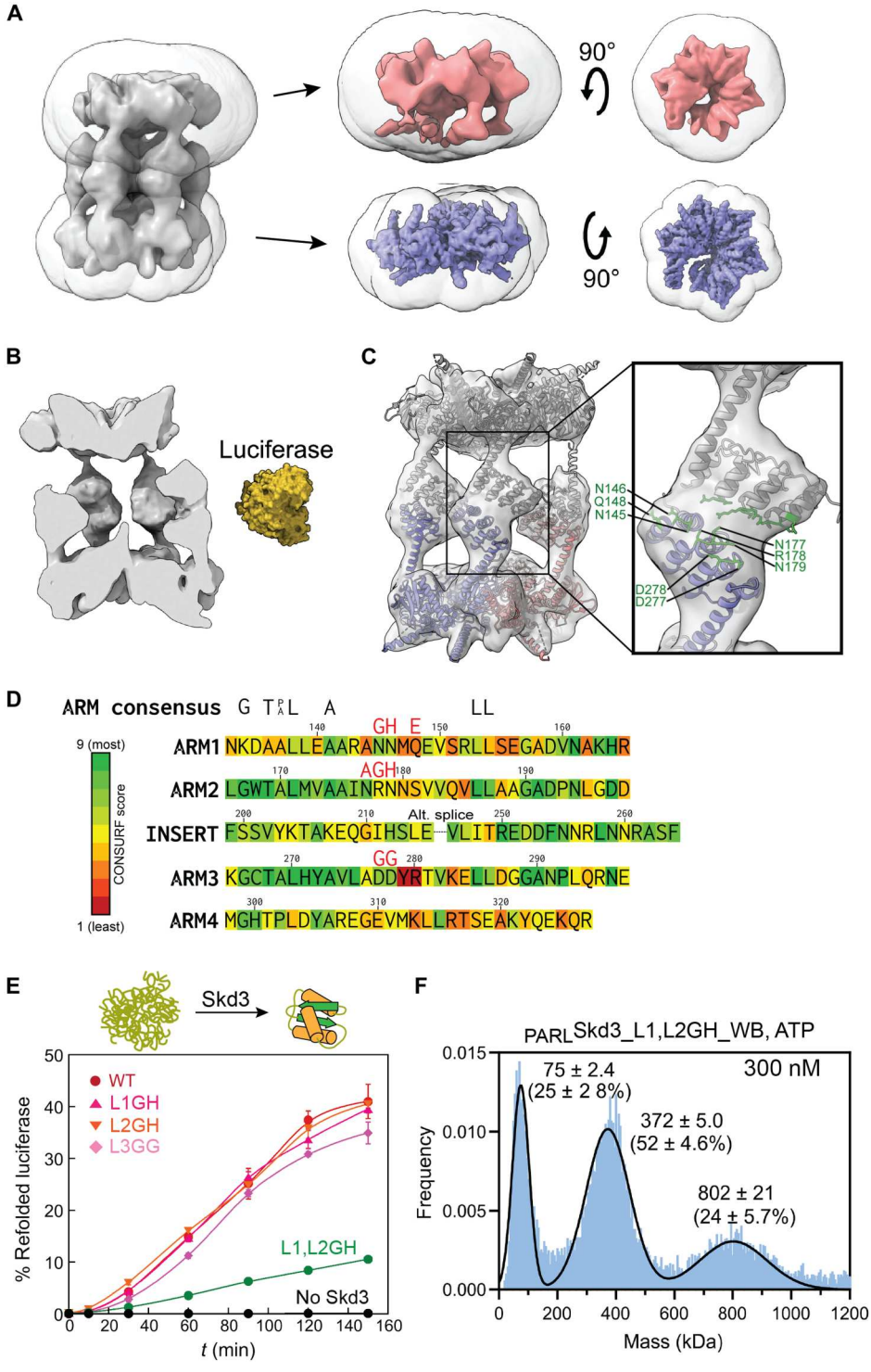

Fig. 3. $_{PARL}$Skd3 dodecamer forms a fenestrated cylindrical cage with the ARD mediating the interface between hexamers. (**A**) Side and face views of the EM density maps of the upper (red) and lower (blue) NBD rings of the Skd3 dodecamer after focused refinement. The masks used for focused refinement are shown. (**B**) Cut-through view of the $_{PARL}$Skd3 dodecamer. Folded luciferase in surface representation [Protein Data Bank (PDB) #1LCI] is shown for comparison. (**C**) Left, overlay of the dodecamer map with model. The molecular model of the open Skd3 NBD (Fig. 2B) was fit as a rigid body to the NBD density. The AlphaFold-predicted model of the ARD-interdomain linker region was fit as a second rigid body to the non-NBD density. Inset, close-up of the ARDs highlighting conserved turn loop residues bridging the dodecamer interface. (**D**) CONSURF analysis of the ARD of human Skd3 isoform 2. Residues are colored by CONSURF scores (*60*) across 791 homologous Skd3 sequences. Mutated turn loop residues are labeled in red. Consensus ARM residues are shown above (black). (**E**) Aggregated luciferase ($U_4L_{0.2}$ protocol) was presented to the indicated Skd3 variants in the presence of 5 mM ATP and ARS, and the generation of enzymatically active luciferase was measured using chemiluminescence (see Materials and Methods). Data are represented as mean ± SD, with n = 3 technical replicates. (**F**) Mass photometry measurements of the assembly state of $_{PARL}$Skd3_L1,L2GH in the presence of 2 mM ATP. The WB mutation was introduced to facilitate hexamer formation. Gaussian fits of the data (black lines) gave the indicated populations in the monomer, hexamer, and dodecamer states and are shown as mean ± SE.

the interface with the clockwise neighboring protomer; R417 and R475 interact with the counterclockwise neighbor. Mutation of these residues is therefore anticipated to disrupt ring assembly. E435 and R417 are also part of the pore 1 and pore 2 loops, respectively, and could help position the pore loops for substrate interactions. Cupo *et al.* (*38*) showed that R417 plays a more important role in Skd3 than in ClpB/Hsp104. M411, H460, C486, and Y567 form the folded core of the large subunit in each protomer, and I682, R650, A591, and G646 stabilize folding of the small subunit. Their mutations are therefore likely to disrupt the folding of the individual NBDs.

The lower resolution of the P1 protomer suggests conformational heterogeneity in the seam protomers. Consistent with this notion, additional EM density was observed at the P1-P6 junction at

Table 1. Summary of the information on cryo-EM data collection and statistics.

Structure				
	Hexamer (high-res)	**Hexamer (closed)**	**Hexamer (open)**	**Dodecamer**
EMDB accession/PDB	PDB ID 7US2 EMD-26722	EMD-26726	EMD-26725	EMD-26728
Data collection				
	Hexamer (high-res)	**Hexamer (closed)**	**Hexamer (open)**	**Dodecamer**
Microscope	Titan Krios G3i			
Detector	Falcon 4			
Voltage (keV)	300			
Energy filter	Selectris			
Data collection software	EPU 2.9			
Pixel size (Å)	0.71 Å			
Total dose	60 e^-/ $Å^2$			
Frame dose	1 e^-/frame			
Defocus	−1 to −2 mm			
Energy filter slit	20 eV			
Tilt (dataset 1A)	0°	0°	0°	0°
Tilt (dataset 1B)	29°	29°	29°	29°
Tilt (dataset 2)	0°	–	–	0°
EM reconstruction				
	Hexamer (high-res)	**Hexamer (closed)**	**Hexamer (open)**	**Dodecamer**
No. of micrographs (dataset 1A)	10,723	10,723	10,723	10,723
No. of micrographs (dataset 1B)	2151	2151	2151	2151
No. of micrographs (dataset 2)	10,854			10,854
Final particle numbers	1,459,443	332,007	519,580	521,193
Resolution at FSC = 0.143 unmasked/masked	3.1/2.76	3.5/3.1	3.3/2.9	6.46/4.40
Map sharpening *B* factor ($Å^2$)	−142.0 (CryoSPARC)	−127.6 (CryoSPARC)	−132.7 (CryoSPARC)	−171.9 (RELION)
Other map sharpening method	DeepEMhancer (high-res model)*	NA	NA	NA
Model				
Composition (#)				
Chains	7			
Atoms	17,200 (hydrogens: 0)			
Residues	2096			
Water	0			
Ligands	MG: 6			
	AGS: 6			
Bonds (RMSD)				
Length (Å) (# > 4σ)	0.005 (0)			
Angles (°) (# > 4σ)	0.694 (0)			
MolProbity score	1.44			
Clash score	3.05			
Ramachandran plot (%)				
Outliers	0.1			
Allowed	4.91			

continued on next page

Model	Hexamer (high-res)	Hexamer (closed)	Hexamer (open)	Dodecamer
Favored	95			
Rotamer outliers (%)	0.56			
Cβ ≤ outliers (%)	0			
Peptide plane (%)				
Cis proline/general	0.0/0.0			
Twisted proline/general	0.0/0.0			
CaBLAM outliers (%)	2.28			
ADP (*B* factors)				
Iso/aniso (#)	17,200/0			
Min/max/mean				
Protein	21.18/148.82/67.33			
Nucleotide	–			
Ligand	21.51/106.17/57.92			
Water	–			
Model versus data				
CC (mask)	0.79			
CC (box)	0.77			
CC (peaks)	0.76			
CC (volume)	0.8			
Mean CC for ligands	0.78			

*For model building of the high-res, the DeepEMhancer sharpened map was used, not the *B* factor sharpened map.

decreased thresholds. 3D variability analysis (3DVA) in CryoSPARC was performed to test this hypothesis, which revealed motions of the seam protomers in the first major variability component (movie S1). 3D classification based on the models generated from 3DVA allowed us to isolate subpopulations of particles in which the NBD ring forms a more closed spiral, which was refined to a resolution of 3.1 Å (Fig. 2E, left, and fig. S6), and a more open spiral, refined to a resolution of 2.9 Å (Fig. 2E, right). The latter is virtually identical to the high-resolution map above (Fig. 2A) and will not be discussed further. In the closed conformation, the P1 and P5 protomers are at the lowest and uppermost positions in the spiral, respectively, and the P6 protomer is mobile and at an intermediate position between P1 and P5 (Fig. 2E, left, and fig. S6C). This closed spiral conformation of Skd3 is similar to that observed by Cupo *et al.* (*38*) and frequently observed among substrate-bound AAA$^+$ ATPases (*18*). Comparison of the closed and open spiral conformations of the Skd3 hexamer revealed ratchet-like motions of the P6 protomer at the seam as it detaches from P1 and moves to the uppermost position in the spiral (Fig. 2E, fig. S6, and movie S1); these movements are conserved among AAA$^+$ ATPases and proposed to provide the force generation mechanism that drives substrate translocation.

At lower thresholds, additional EM density corresponding to the N-terminal domains of Skd3 was observed. For P1 to P5, EM density was observed for the N-terminal ARDs and the interdomain linker (residues 310 to 336), with the strongest density in the C-terminal half of the linker closer to the NBD. This allowed an AlphaFold-predicted model of the Skd3 ARD and the linker region (minus residues 198 to 267, which comprise an insertion domain in the ARD) to be docked as a rigid body into the cryo-EM density (Fig. 2F), suggesting that the linker forms a relatively rigid helix that positions the ARDs and may mediate interdomain communication with the NBDs. Nevertheless, the resolution reduces significantly midway through the interdomain helix, likely reflecting flexibility in the hinge between this helix and the ARD or disorder in the N-terminal end of the linker. EM density for the ARD of P6 is weaker and cannot be fit, suggesting higher flexibility of the ARD and the interdomain linker for the protomer at the uppermost position of the spiral (Fig. 2F and fig. S4B). In summary, high-resolution structures of both the closed and open spiral conformations of the Skd3 hexamer reveal ratchet-like motions of the seam protomers that are implicated in driving substrate translocation, visualize the nucleotide state of an AAA$^+$ ATPase in the open spiral conformation, and suggest the molecular basis of disease-linked Skd3 mutations.

Dodecameric $_{PARL}$Skd3 forms a fenestrated cage

During cryo-EM data analysis in CryoSPARC, we found that the 3D classification and refinement algorithms were heavily biased toward optimizing the alignment of the NBD but did not effectively recover dodecamer particles or separate them from hexamers. In contrast, classification of the 2D images in RELION allowed in silico purification of the $_{PARL}$Skd3 dodecamers, which was refined to an overall resolution of 6.5 Å (Fig. 1E, figs. S2 and S7, and Table 1). The local resolution varied from ~4 Å for the designated lower NBD ring, ~8 Å in the ARDs, to 8 to 12 Å in the upper NBD ring (fig. S7A). Strong

density could be observed for the C terminus of the interdomain helix connecting to the lower NBD ring (fig. S7A). Local resolution drops significantly midway through the interdomain helices in the lower hexamer, likely reflecting increased conformational flexibility in the linker as was observed in the hexamer structure. The lower local resolution of the upper hexamer further suggests that the dodecamer interface is dynamic, which would lead to variations in the relative orientation of the two hexamers and blurring of the upper hexamer density if the refinement optimizes the alignment of the lower NBD ring. To test this hypothesis, we carried out focused refinement of the upper and lower NBD rings. This resulted in improved resolutions, with the lower NBD ring refined to 3.8 Å and the upper NBD ring refined to 7.7 Å (Fig. 3A). The spiral conformation can be discerned in both NBD rings.

The Skd3 dodecamer forms a fenestrated cylindrical cage, 130 Å in diameter and 180 Å in height, and is comparable in size to the GroEL tetradecamer and TRiC hexadecamer (fig. S7F). Unlike GroEL, which consists of two heptameric rings stacked back-to-back, the interior of the dodecamer forms a contiguous large cavity sufficient to fit a globular protein/complex of ~70 kDa, such as the model protein luciferase used in refolding studies (Fig. 3B). In addition, unlike GroEL and TRiC, in which the internal cavity is sealed from solvent upon lid closing, the cavity in Skd3 is fenestrated and open to surrounding solvent, with gaps between the neighboring ARDs and interdomain helices that allow diffusion of solvent and small molecules while blocking the entry or exit of most globular proteins.

Despite regions with low resolution, the reconstruction shows that the $_{PARL}$Skd3 dodecamer is composed of head-to-head dimers of two opposing hexamers, with the ARDs mediating contacts at the interface between the two hexamers (Fig. 3C). The density for the ARDs is clearest in protomers P2 to P4, allowing an AlphaFold-predicted model for the ARD and interdomain helix region to be docked as a rigid body into these densities (Fig. 3C). The docking model suggests that the dodecamer interface is mediated in part by "side-to-side" interactions of the ARDs from the opposing hexamers via residues in the "turn loops" of the ankyrin repeat motifs (ARMs), including ^{145}NN in ARM1, ^{177}NRN in ARM2, and ^{277}DD in ARM3 (Fig. 3C, inset). These residues are conserved or semi-conserved among Skd3 homologs (Fig. 3D and fig. S8A) but are distinct from the consensus sequence (GH) at the turn loops of most ARDs (*44*).

To test the role of these contacts in Skd3 dodecamer formation, we replaced the turn loop residues in ARM1 and ARM2 with the consensus sequence (named mutants L1GH and L2GH) and the turn loop Asp residues in ARM3 with GG (mutant L3GG). Using the reactivation of aggregated luciferase as an initial screen for the mutational effects on Skd3 activity, we found that mutation of the individual turn loops had either no effect or a modest effect on Skd3's chaperone activity (Fig. 3E and fig. S8B). However, combining the L1GH and L2GH mutations resulted in a three- to fourfold reduction in luciferase reactivation (Fig. 3E and fig. S8B, green). Although the yield of luciferase refolding varied depending on how the aggregate was generated, the mutational effects of turn loop residues were the same regardless of the nature of the aggregates (Fig. 3E and fig. S8B). Mass photometry measurements of the double mutant, Skd3_L1,L2GH, showed that its dodecamer formation was impaired (Fig. 3F versus Fig. 1B). In the presence of ATP, the ratio of dodecamer relative to hexamer was reduced from 0.91 ± 0.07 with Skd3_WB (Fig. 1B) to 0.41 ± 0.12 with Skd3_L1,L2GH_WB (Fig. 3F). In addition, as shown later (section "Dodecamer assembly–deficient Skd3 mutants uncouple disaggregation from client refolding"), steric blocks at the N terminus of $_{PARL}$Skd3 impaired Skd3 dodecamer formation without affecting the hexamer. Together, these results support the role of the ARDs in mediating dodecamer formation and suggest that the conserved Asn residues in the ARD turn loops mediate hydrogen bonding interactions that form part of the dodecamer interaction interface.

Client protein undergoes protected folding on $_{PARL}$Skd3

$_{PARL}$Skd3 is an efficient chaperone that can generate enzymatically active luciferase from its aggregates in the absence of additional chaperones that promote folding [Figs. 3 and 4 and (*27*)]. This activity and the observation of the internal cavity in dodecameric $_{PARL}$Skd3 (Fig. 3B) led us to ask whether $_{PARL}$Skd3 provides a protected environment for folding in addition to acting as a disaggregase. We addressed this question by challenging the $_{PARL}$Skd3-mediated luciferase refolding reaction with GroEL-D87K, which irreversibly binds unfolded polypeptides and early folding intermediates (*45*) and thus serves as a conformational probe for the folding state of the client protein released from the chaperone. In the continuous extraction model established for ClpB/Hsp104, client proteins such as luciferase are extracted from the aggregate by continuous threading through the pore ring and are released in an unfolded conformation, which can refold either spontaneously or with the assistance of other chaperones (Fig. 4A, lower pathway) (*15*, *16*). If $_{PARL}$Skd3 acts solely via this mechanism, GroEL-D87K will be an effective inhibitor of luciferase refolding by sequestering the unfolded client protein released from the disaggregase (Fig. 4A, lower pathway), as was shown for ClpB (*15*, *16*). In contrast, if luciferase reaches a committed stage of folding on $_{PARL}$Skd3 before it is released from the chaperone, the refolding reaction would be insensitive to the presence of GroEL-D87K (Fig. 4A, upper pathway).

To distinguish between these models, we measured the kinetics of reactivation of aggregated luciferase, which includes both the disaggregation and refolding reactions. $_{PARL}$Skd3 mediates efficient reactivation of aggregated luciferase (Fig. 4A), as reported previously (*27*). Up to 1 μM GroEL-D87K, added either simultaneously with $_{PARL}$Skd3 or after mixing $_{PARL}$Skd3 with luciferase aggregates, affected the yield of the reaction by only 10 to 20% (Fig. 4B and fig. S9A). Regardless of how the luciferase aggregate was generated, all the luciferase reactivation reactions mediated by $_{PARL}$Skd3 were impervious to GroEL-D87K (Fig. 4B and fig. S9A). These results strongly suggest that unfolded luciferase molecules are strongly protected from external chaperones by $_{PARL}$Skd3, and further, they reach a conformation committed to folding before release from this chaperone.

As controls, we tested the effectiveness of GroEL-D87K in reactions that allow luciferase to fold from the denatured state, by dilution of GdmHCl-denatured luciferase into aqueous solution to concentrations below 50 nM. Under these conditions, a fraction of denatured luciferase underwent spontaneous folding, which was abolished by 320 nM GroEL-D87K (Fig. 4C, black versus blue), supporting GroEL-D87K as an effective trap for unfolded proteins. Refolding of denatured luciferase was enhanced by $_{PARL}$Skd3 (Fig. 4C, red versus black); however, when denatured luciferase was presented simultaneously to $_{PARL}$Skd3 and

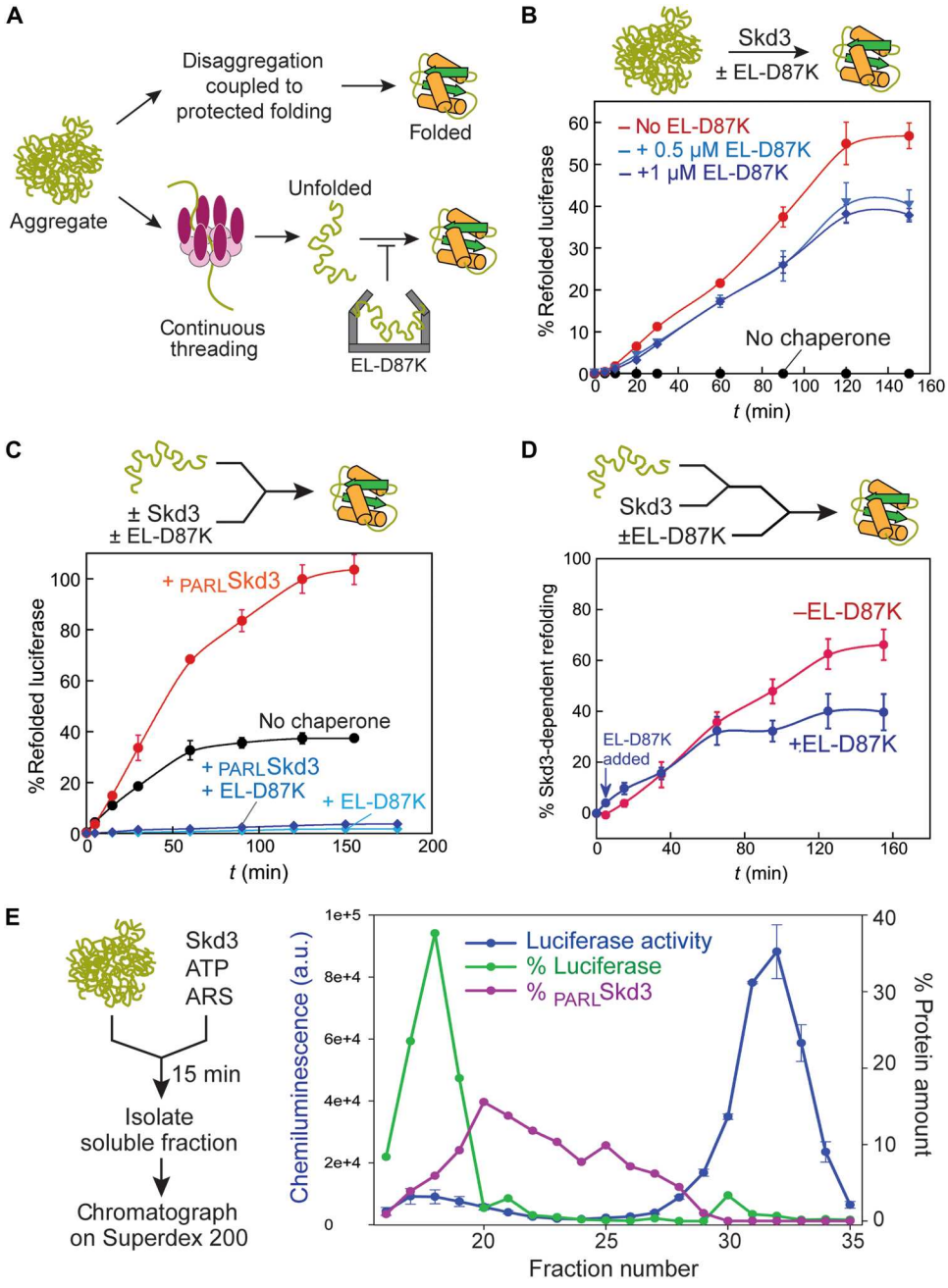

Fig. 4. $_{PARL}$Skd3 releases luciferase in a conformation committed to folding. (**A**) Alternative models for luciferase disaggregation and refolding mediated by $_{PARL}$Skd3 and the use of GroEL-D87K to distinguish between the models. (**B**) Refolding of aggregated luciferase ($U_4L_{0.2}$ protocol) by $_{PARL}$Skd3 was measured as in Fig. 3E in the presence and absence of the indicated concentrations of GroEL-D87K. (**C**) Luciferase denatured in 5 M GdmHCl was diluted to 50 nM in refolding buffer. Where indicated, the reaction also contained 1 μM $_{PARL}$Skd3 and/or 320 nM GroEL-D87K. Refolded luciferase was detected by chemiluminescence. (**D**) Luciferase denatured in 5 M GdmHCl was diluted to 50 nM in refolding buffer containing 1 μM Skd3; where indicated, 320 nM GroEL-D87K was added 5 min later, and refolding was measured by chemiluminescence. Spontaneous luciferase refolding with and without GroEL-D87K was measured in parallel and subtracted. (**E**) Aggregated luciferase ($U_8L_{0.5}$ protocol) was mixed with 1 μM $_{PARL}$Skd3 in the presence of 5 mM ATP and ARS to initiate disaggregation and refolding. Fifteen minutes later, soluble proteins were chromatographed on a Superdex 200 column, and 0.5 ml fractions was collected and analyzed. Enzymatically active luciferase in individual fractions was detected using chemiluminescence (blue). Individual fractions were also probed with anti-His (for luciferase, green) and anti-ClpB (for Skd3, magenta) antibodies. See fig. S9 for raw data. Data are shown as mean ± SEM in (B) to (D) or mean ± SD in (E), with $n = 3$ technical replicates. Error bars are plotted but may not be visible.

GroEL-D87K, refolding was abolished (Fig. 4C, red versus navy), indicating that GroEL-D87K outcompetes $_{PARL}$Skd3 in binding unfolded luciferase. In contrast, when denatured luciferase was preloaded on $_{PARL}$Skd3 followed by addition of GroEL-D87K, Skd3-dependent luciferase refolding was strongly protected, especially at early times (Fig. 4D). This observation is similar to the protection of luciferase in the coupled disaggregation-refolding reaction (Fig. 4B), and together, they strongly suggest that folding of luciferase can occur on $_{PARL}$Skd3 in a highly protected manner. As additional controls, Hsp104/40/70-mediated reactivation of aggregated luciferase was sensitive to GroEL-D87K (fig. S9, B and C), analogous to observations with ClpB/DnaKJ (*15*, *16*). Luciferase reactivation mediated by the potentiated mutant Hsp104_A503S, which bypasses the Hsp40/70 requirement (*46*), was also abolished by GroEL-D87K (fig. S9D). Together, these results show that Skd3-mediated luciferase reactivation uses a mechanism distinct from the continuous threading model established for ClpB/Hsp104, and strongly suggest that luciferase molecules released from $_{PARL}$Skd3 are in a conformation committed to folding.

To provide independent evidence that luciferase folding can initiate when bound to $_{PARL}$Skd3, we analyzed the protein complexes generated during the refolding reaction. The coupled luciferase disaggregation-refolding reaction was chilled at 4°C for 15 min after its initiation. Large aggregates were removed by centrifugation, and soluble protein/complexes of different sizes were separated by gel filtration chromatography and analyzed immediately upon elution (Fig. 4E). Significant luciferase activity was detected both in high molecular weight fractions that correspond to Skd3 oligomers (fractions 17 to 20 or 8.5- to 10-ml elution volume) and in low molecular weight fractions that correspond to free luciferase monomer (fractions 28 to 34 or 14- to 17-ml elution volume) (Fig. 4E, blue). In contrast, luciferase activity was detected only in the late fractions for reactions with $_{PARL}$Skd3_WB or without chaperone at levels 200-fold below that of the reaction with $_{PARL}$Skd3 (fig. S9, E and F). The cofractionation of luciferase activity with Skd3 oligomers strongly suggests that a fraction of luciferase acquires either the native state or a folding-competent conformation when bound to $_{PARL}$Skd3. Western blot analysis showed that most luciferase protein eluted in the high molecular weight fractions associated with $_{PARL}$Skd3 oligomers (Fig. 4, E and F, green, and fig. S9, G to I), whereas most enzymatically active luciferase was detected in the unbound fractions (Fig. 4, E and F, blue). This further suggests that luciferase molecules that have been solubilized but not yet folded remain stably bound to Skd3 oligomers and are more promptly released from Skd3 when they reach a folding-competent conformation.

Together, the results of this section show that $_{PARL}$Skd3 acts via a mechanism distinct from the continuous extraction model that describes the ClpB/Hsp104 disaggregase systems. Instead, solubilized client proteins remain stably bound to and protected by $_{PARL}$Skd3 and can undergo folding before their release from $_{PARL}$Skd3.

Dodecamer assembly–deficient Skd3 mutants uncouple disaggregation from client refolding

We next asked whether formation of the Skd3 dodecamer is involved in the protected folding of clients on Skd3 by examining Skd3 mutants defective in dodecamer assembly. The reduced activity of Skd3_L1,L2GH in the coupled disaggregation-refolding reaction suggested a role of the dodecamer in the chaperone activity of Skd3 (Fig. 3). As the defect of this mutant is modest, we sought to further disrupt dodecamer assembly by introducing N-terminal extensions to $_{PARL}$Skd3 that could act as steric blocks. In support of this notion, fusion of the SUMO moiety to $_{PARL}$Skd3 abolished dodecamer formation (fig. S10A). $_{MPP}$Skd3, which retains a 30–amino acid inhibitory sequence N-terminal to $_{PARL}$Skd3 (Fig. 1A) and (*27*), showed heterogeneous assembly in mass photometry measurements (fig. S10B). However, $_{MPP}$Skd3 displayed Skd3 concentration–dependent ATPase activation with rates within twofold of that of $_{PARL}$Skd3 [fig. S10C and (*27*)], consistent with its ability to assemble ATPase-active hexamers. This suggests that the behavior of $_{MPP}$Skd3 in mass photometry was not due to its inability to form hexamers but to poor biophysical properties. Physiologically, $_{MPP}$Skd3 needs to associate with the mitochondrial inner membrane to gain access to the PARL protease and likely has a propensity to bind to hydrophobic surfaces, which may complicate surface-based mass photometry measurements. We therefore tested deletions of various regions of the inhibitory sequence to improve its stability in solution (MPPΔ1, MPPΔ2, and MPPΔ3; fig. S10D). All three mutants displayed substantially reduced activity in the coupled luciferase disaggregation-refolding reaction, as did $_{MPP}$Skd3 [Fig. 5A, fig. S10E, and (*27*)]. $_{MPP\Delta1}$Skd3 was prone to aggregation during purification, and $_{MPP\Delta2}$Skd3 remained poorly behaved on mass photometry (fig. S10F); these mutants were therefore not pursued further. In contrast, $_{MPP\Delta3}$Skd3, in which the C-terminal hydrophobic residues in the inhibitory sequence were removed, was well expressed and soluble. Mass photometry measurements showed that this mutant assembled efficiently into hexamers but was strongly impaired in dodecamer formation compared to $_{PARL}$Skd3 (Fig. 5, B and C).

We tested whether the reduced chaperone activities of Skd3_L1,L2GH and $_{MPP\Delta3}$Skd3, which are specifically defective in dodecamer assembly, were due to impaired disaggregase activity or to less efficient client refolding. To this end, we measured and compared the efficiencies by which wild-type and mutant Skd3 solubilize luciferase aggregates. Preformed luciferase aggregates were incubated with Skd3 and, at various times, the reaction was quenched using apyrase, and soluble and aggregated proteins were separated by centrifugation and visualized by Western blot analysis. These measurements showed that both mutants solubilized luciferase aggregates with efficiencies and kinetics comparable to wild-type $_{PARL}$Skd3 (Fig. 5, D and E), indicating that the defect of these mutants in luciferase reactivation was not due to impaired disaggregase activity but rather can be attributed to reduced refolding efficiency.

If the Skd3 dodecamer mediates protected refolding of luciferase, a prediction is that the dodecamer assembly–deficient mutants no longer protect the refolding reaction from GroEL-D87K. This was indeed the case: Luciferase reactivation by Skd3_L1,L2GH and $_{MPP\Delta3}$Skd3 decreased by over twofold in the presence of 320 nM GroEL-D87K and was reduced to background levels (1.5 and 1.4% refolded luciferase, respectively) in the presence of 3 μM GroEL-D87K (Fig. 5, F to H). In contrast, the reaction with wild-type $_{PARL}$Skd3 was reduced only ~10% by 320 nM GroEL-D87K and ~50% by 3 μM GroEL-D87K (Figs. 4 and 5G). We also note that neither mutant completely abolished dodecamer formation (Figs. 3F and 5, B and C); therefore, the observations with these mutants provide a lower limit for the sensitivity of the Skd3 hexamer–mediated luciferase refolding reaction to GroEL-D87K.

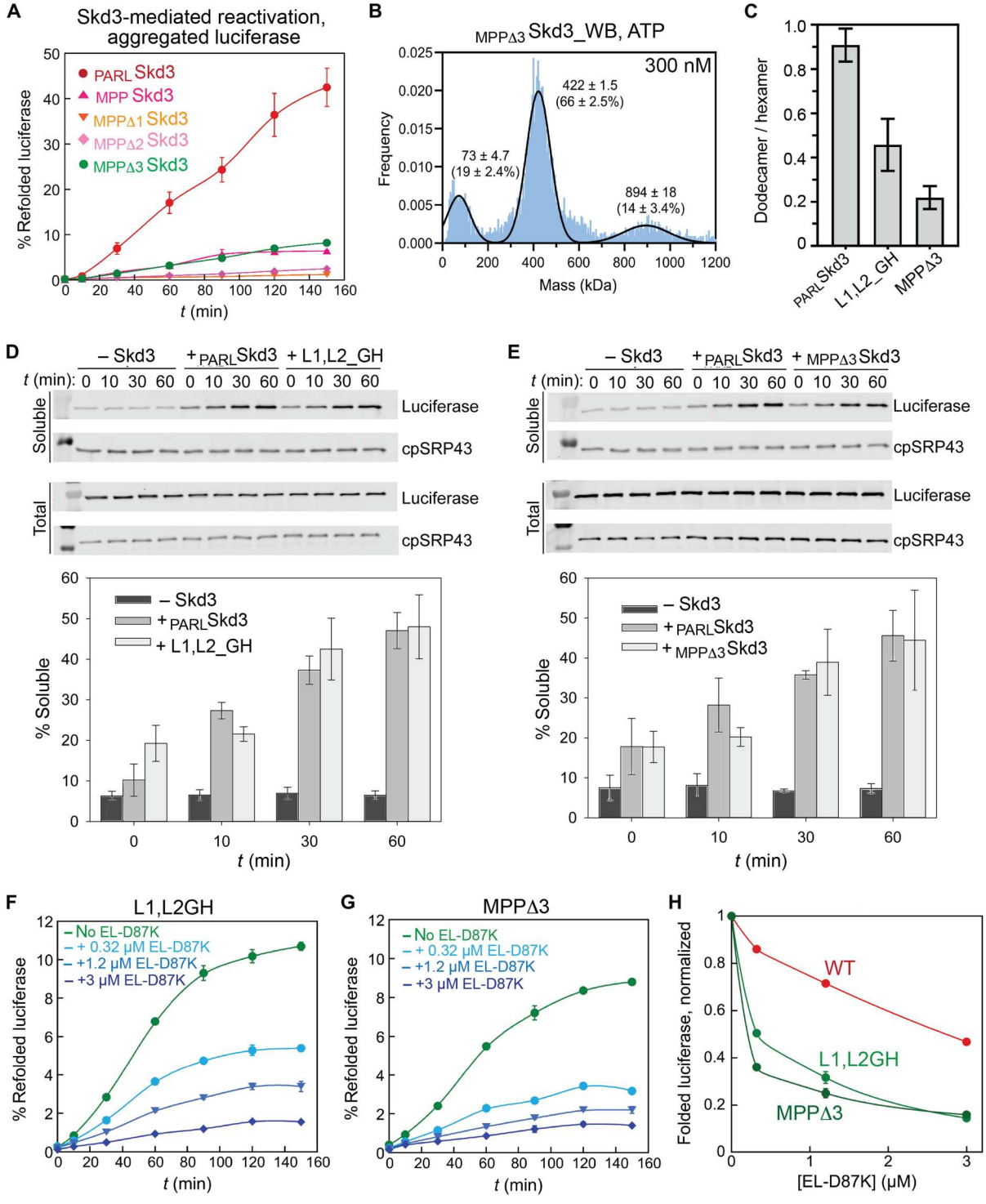

Fig. 5. Dodecamer assembly–deficient mutants uncouple client refolding from disaggregation. (**A**) Refolding of aggregated luciferase mediated by the indicated Skd3 variants, measured as in Fig. 3E. (**B**) Mass photometry measurement of $_{MPP\Delta3}$Skd3_WB in the presence of 2 mM ATP. Gaussian fits of the data (black lines) gave the indicated population in the monomer, hexamer, and dodecamer states. (**C**) Summary of the dodecamer/hexamer population ratio for $_{PARL}$Skd3 and the dodecamer assembly–defective Skd3 mutants. (**D** and **E**) Disaggregation of luciferase by $_{PARL}$Skd3, Skd3_L1,L2GH (D), and $_{MPP\Delta3}$Skd3 (E) was measured as described in Materials and Methods. Top, representative Western blot analysis of the soluble and total luciferase; bottom, quantification of the data. cpSRP43, a plant-derived protein, was used as a loading control. (**F** and **G**) Refolding of aggregated luciferase ($U_4L_{0.2}$ protocol) by Skd3_L1,L2GH (F) and $_{MPPD3}$Skd3 (G) was measured as in Fig. 3D in the absence and presence of the indicated concentrations of GroEL-D87K. (**H**) The effect of GroEL-D87K on luciferase refolding is compared between wild-type $_{PARL}$Skd3 (red), Skd3_L1,L2GH (green), and $_{MPP\Delta3}$Skd3 (dark green). The amount of refolded luciferase at 150 min for reactions containing GroEL-D87K was normalized to that without the trap for each Skd3 variant. Data are shown as mean ± SEM in (A) and (F) to (H) or mean ± SD in (D) and (E), with $n = 3$ technical replicates. Error bars are plotted but may not be visible.

If client proteins fold within the $_{PARL}$Skd3 dodecamer, another prediction is that proteins whose size exceeds the dimension of the dodecamer cavity cannot be efficiently refolded by this chaperone. To test this model, we examined the refolding of β-galactosidase (β-Gal), which has a monomeric molecular weight of 115 kDa and an elongated structure in the folded monomer, making it incompatible to fit in the internal cavity of the Skd3 dodecamer. $_{PARL}$Skd3 reactivated preaggregated β-Gal by only 4% above background levels (fig. S11A). Since this reaction requires Skd3 to both solubilize the aggregate and refold β-Gal, we further measured the refolding of urea-denatured β-Gal, which minimizes contributions from the aggregate solubilization step. Skd3 increased the refolding of urea-denatured β-Gal by only 15 to 20% above that of the spontaneous reaction (fig. S11B). These observations contrast with those with Hsp104/40/70, which can efficiently refold aggregated β-Gal (*47*). While the repertoire of client proteins that can be refolded by Skd3 remains to be determined, these observations are consistent with the dimension of the dodecamer cavity, which likely imposes a size limit on the client proteins that can undergo protected refolding on Skd3.

Collectively, the results in this section show that disaggregase activity can be uncoupled from protected client refolding in dodecamer assembly–deficient Skd3 mutants. Thus, the Skd3 hexamer is sufficient for disaggregase activity, whereas efficient and protected client refolding requires assembly of the Skd3 dodecamer.

The ARD can mediate substrate interactions

In the molecular model for the Skd3 dodecamer, multiple conserved hydrophobic and aromatic residues on the concave face of the Skd3 ARD and on an insertion domain between ARM2 and ARM3 (residues 198 to 267 in isoform 1) together form a hydrophobic groove that lines the internal cavity (Fig. 6A). Mutation of hydrophobic residues that constitute this surface to Ala or Gly impaired luciferase reactivation by $_{PARL}$Skd3 (Fig. 6A). In addition, three MGCA-linked mutations in Skd3 (Y272C, T268M, and A269T) are located at this hydrophobic surface (Fig. 6A); these mutations also severely disrupted $_{PARL}$Skd3-mediated luciferase refolding (Fig. 6B). These observations support an important role of this hydrophobic groove in the chaperone function of Skd3.

These observations led us to ask whether the Skd3 ARD directly participates in substrate interactions. To probe the interaction of Skd3 with unfolded polypeptides, we used the model substrate casein, which exists predominantly in a disordered state. Equilibrium titrations based on the anisotropy of fluorescein isothiocyanate (FITC)–labeled casein showed that in the presence of ATPγS, $_{PARL}$Skd3 and $_{PARL}$Skd3_WB bound FITC-labeled casein with modest affinity, with equilibrium dissociation constants (K_d) of 3.4 and 3.6 μM, respectively (Fig. 6D). Unexpectedly, in the absence of ATP or ATP analogs, where $_{PARL}$Skd3 is predominantly monomeric (fig. S1E), FITC-casein was bound with a K_d value of 0.86 μM (Fig. 6D). The smaller anisotropy change of FITC-casein at saturating concentrations of apo- versus ATPγS-bound $_{PARL}$Skd3 was consistent with a smaller number of FITC probes in casein that are immobilized by binding of the $_{PARL}$Skd3 monomer than oligomer. In the presence of ATP and the ATP regeneration system (ARS), which allows ATP binding and hydrolysis, the observed binding affinity and anisotropy change was in between the ATPγS and apo states (Fig. 6D). The isolated ARD also bound to FITC-casein with a K_d value of 3.7 μM (Fig. 6D), within fivefold of that of apo-Skd3. Thus, the ARD can directly participate in interaction with an unfolded polypeptide.

To independently assess the participation of the ARD in substrate interactions, we tested whether it can prevent the aggregation of the amyloid β (Aβ42) peptide, a proteolytic fragment of the amyloid precursor protein that is highly prone to aggregation. To compare the activity of ARD with $_{PARL}$Skd3 in the same oligomeric state, we carried out the reactions without added ATP and ARS such that $_{PARL}$Skd3 would be predominantly monomeric. $_{PARL}$Skd3 effectively reduced the extent and delayed the kinetics of amyloid formation by Aβ42 under these conditions (Fig. 6E). Substantial inhibition of Aβ42 was observed at 0.1 μM $_{PARL}$Skd3, $^{1}/_{50}$ of the concentration of Aβ42, suggesting high-affinity recognition (Fig. 6, E and G). The ARD also delayed Aβ42 aggregation, albeit about fivefold less efficiently compared to $_{PARL}$Skd3 (Fig. 6, F and G). The ability of $_{PARL}$Skd3 and ARD to reduce Aβ42 fibril formation was corroborated by transmission EM (TEM) analysis (Fig. 6H). Mutants L1,L2GH and MPPΔ3 inhibited Aβ42 aggregation as effectively as $_{PARL}$Skd3 (Fig. 6H and fig. S12), indicating that these mutations specifically disrupt the dodecamer interface (Fig. 5) but are unlikely to impair interaction with hydrophobic regions of substrate proteins. In contrast, mutant 246-249A was less effective in inhibiting Aβ42 aggregation (Fig. 6G and fig. S12), supporting its role as a putative substrate contact site on the ARD (Fig. 6A). Thus, $_{PARL}$Skd3 can protect unstructured and hydrophobic polypeptides from forming irreversible aggregates under ATP-depleted conditions. Moreover, these results provide additional evidence that the Skd3 ARD participates in client interactions that shield hydrophobic regions of a protein from aggregation.

DISCUSSION

Skd3 is an AAA$^+$ chaperone that can efficiently reactivate aggregated model substrates and may serve as the missing general chaperone in the mitochondrial IMS, a crowded space with diverse and challenging proteostatic demands. However, the molecular mechanisms that give rise to the remarkably effective chaperone activity of Skd3 remain elusive, and its precise roles in mitochondria remain to be determined. In this work, the combination of structural and biochemical analysis strongly suggests that Skd3 is a multifunctional chaperone that not only acts as a disaggregase, as previously described (*27*), but also can further provide a protected environment for client folding via dodecamer assembly. Our results suggest a model for how a molecular chaperone couples the disaggregation of client proteins to their refolding, and thus provides an effective repair mechanism for misfolded, aggregated proteins.

The Skd3 NBD is highly homologous to NBD2 of ClpB and Hsp104. High-resolution cryo-EM structures of the $_{PARL}$Skd3 hexamer here showed that the Skd3 NBD alternates between open and closed spiral conformations (Fig. 2). The closed spiral conformation, also reported by Cupo *et al.* (*38*), resembles the structures observed for many protein-remodeling AAA$^+$ ATPases (*18*–*20*, *48*), in which the pore loops of protomers P1 to P5 contact the bound substrate in a spiral staircase arrangement, whereas the P6 "seam" protomer is detached (Fig. 7, inset). The open spiral conformation of $_{PARL}$Skd3 is less often observed but is structurally similar to the "extended" spiral observed for Hsp104-NBD2 bound to casein (*19*). In this conformation, the P6 protomer adopts the uppermost position in the spiral staircase and advances contact with the substrate

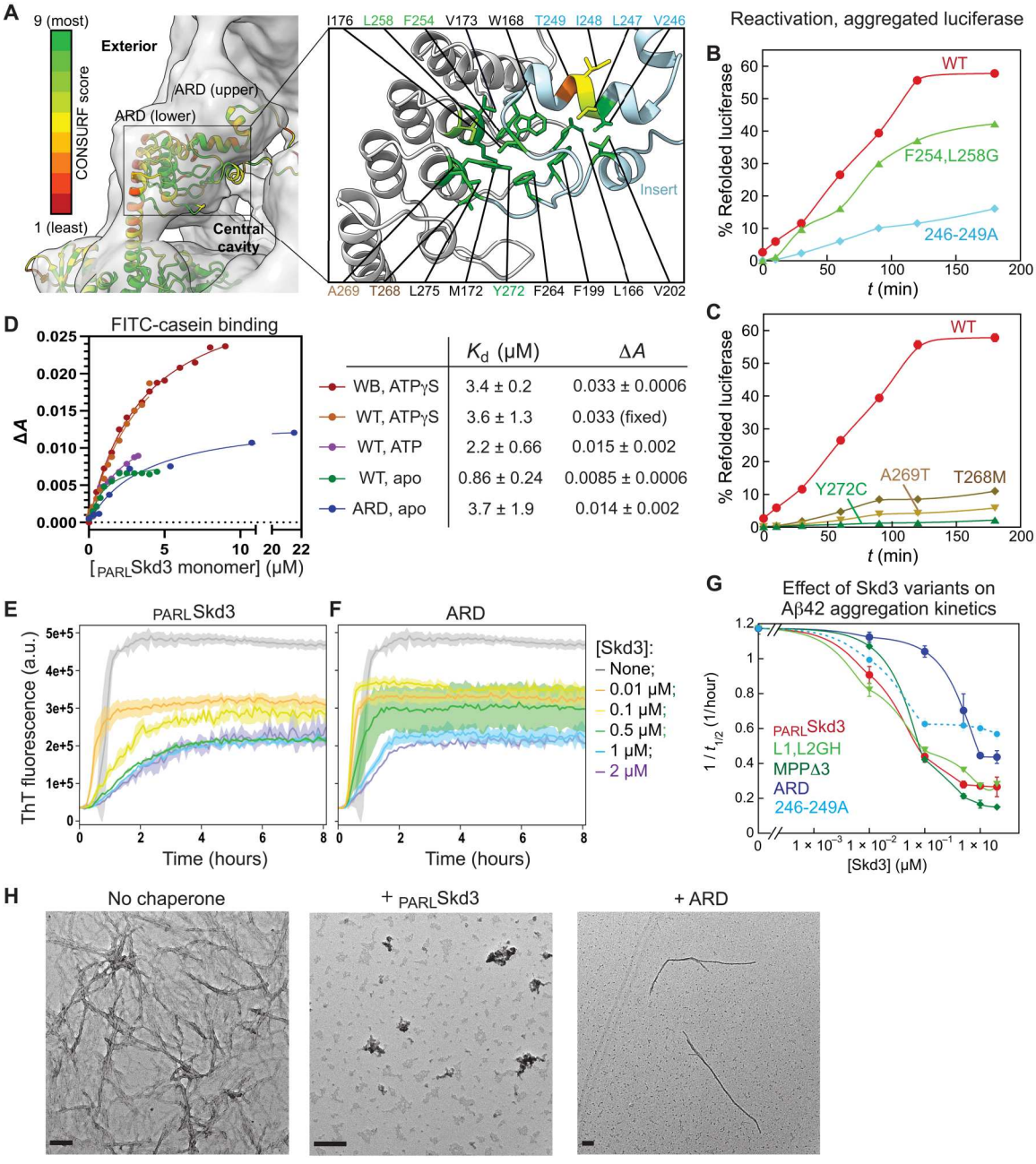

Fig. 6. Skd3 ARD can participate in substrate interaction. (**A**) Side view of the ARD showing the surface that faces the internal cavity in the Skd3 dodecamer. Color coding for CONSURF scores is the same as in Fig. 3. In the inset, conserved hydrophobic residues (CONSURF ≥ 6) on the surface of the ARD (gray) and the insertion domain (aqua) are highlighted. Residues tested by mutagenesis in (B) and (C) are color-indicated. (**B** and **C**) Refolding of aggregated luciferase mediated by the indicated Skd3 variants, measured as in Fig. 3E. (**D**) Equilibrium titrations to measure the binding of FITC-casein to $_{PARL}$Skd3 and ARD in the indicated nucleotide states. Lines are fits of the data to Eq. 2, and the obtained K_d values are summarized. (**E** and **F**) $_{PARL}$Skd3 and ARD delay Aβ42 fibrillation under ATP-depleted conditions. Monomeric Aβ42 (5 μM) was incubated with and without the indicated concentrations of $_{PARL}$Skd3 (E) or ARD (F) under quiescent conditions without added ATP and ARS. Fibril formation was monitored by ThT fluorescence every 5 min. The dark lines show the mean of three replicates, and the shaded area shows the range of data. The data were analyzed by the AmyloFit algorithm, from which fibrillation reaction halftimes were extracted and summarized in (G). (**G**) Summary of the effect of $_{PARL}$Skd3 variants on the kinetics of Aβ42 fibrillation. "$t_{1/2}$" denotes the half-time of Aβ42 fibrillation so that $1/t_{1/2}$ represents the apparent rate constant of the reaction. Data are shown as mean ± SEM, with n = 3 technical replicates. See fig. S12 for raw data. (**H**) Aβ42 fibrillation reactions were carried out with and without 2 μM of indicated chaperone. Reactions were imaged under TEM after 6 hours. Scale bar, 100 nm.

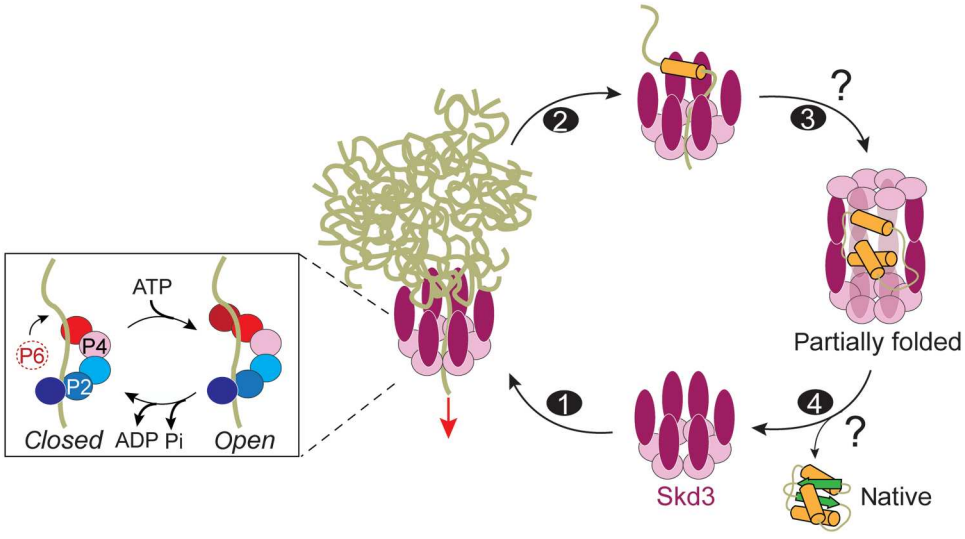

Fig. 7. Working model for the coupled disaggregation and refolding reaction mediated by $_{PARL}$Skd3. Step 1, an Skd3 hexamer recognizes aggregated proteins and initiates substrate extraction. Step 2, an Skd3-bound substrate protein is dislodged from the aggregate. Step 3, Skd3 dodecamer assembles, and substrate protein initiates folding in the internal cavity. Step 4, substrate protein, either folded or in a folding-competent conformation, is released from Skd3 upon dodecamer disassembly. The inset shows the movement of the seam protomer (P6) from the lowest to the uppermost position as the NBD hexamer rearranges from the closed to the open spiral conformation, which generates a mechanical force that "pulls" the substrate polypeptide in the downward direction (red arrow). The question marks denote that the molecular mechanism underlying the transitions is still unclear.

polypeptide by two additional amino acids (Fig. 7, inset). The open spiral conformation is likely favored by high ATP occupancy and thus captured by the combination of WB mutation and slowly hydrolyzing ATPγS in this study. Collectively, these structures are consistent with the conserved force-generation mechanism of protein-threading AAA$^+$ proteins, in which the seam protomer transitions through the closed spiral conformation as it moves from the lowest to the uppermost position of the open spiral during each ATPase cycle. This movement allows the NBD ring to move "up" the substrate polypeptide, generating a force that propels substrate translocation (Fig. 7, inset). These structural observations, together with the requirement of pore loop and ATPase active-site residues for Skd3-mediated disaggregation (*27*), suggest that the Skd3 hexamer harbors most of the molecular features to act as a disaggregase by threading substrate proteins through the pore ring (Fig. 7, steps 1 and 2).

Nevertheless, multiple observations here demonstrate that disaggregation via continuous substrate threading, established for ClpB/Hsp104, is insufficient to explain how $_{PARL}$Skd3 efficiently reactivates aggregated luciferase. The coupled disaggregation-refolding reaction mediated by $_{PARL}$Skd3 is strongly protected from GroEL-D87K, which traps unfolded polypeptides and early folding intermediates (Fig. 4), indicating that luciferase molecules released from $_{PARL}$Skd3 are in the native or near-native conformation. This contrasts with the ClpB (*15*, *16*) and Hsp104 (fig. S9, B to D) systems, which are sensitive to the GroEL-D87K trap, and excludes models in which the substrate protein is completely threaded through the Skd3 pore ring. Instead, this observation suggests that partial threading is sufficient to dislodge substrate proteins from the aggregate, as has been observed in some cases with ClpB (*49*) and Hsp104 (*50*). The resistance of the $_{PARL}$Skd3-mediated refolding reaction to GroEL-D87K also excludes models in which substrates are folded via multiple cycles of binding and release by Skd3, which would expose unfolded proteins susceptible to GroEL-D87K. Last, gel filtration chromatography analysis of reaction intermediates showed that solubilized substrates remain stably associated with $_{PARL}$Skd3 oligomers, and a fraction of substrates acquired the native or near-native conformation when bound to $_{PARL}$Skd3 (Fig. 4E). Collectively, these data support a model in which aggregate solubilization is tightly coupled to the initiation of client refolding in a protected environment provided by $_{PARL}$Skd3.

The results here further suggest that client refolding is facilitated by Skd3 dodecamer assembly. Skd3 mutants that disrupt the dodecamer interface retain disaggregase activity but specifically impair the refolding of luciferase (Fig. 5). This and the higher susceptibility of these mutants to GroEL-D87K show that while the hexamer is necessary and sufficient for disaggregation, protected client refolding depends on formation of the Skd3 dodecamer. A recent report also showed that Skd3 dodecamer assembly is correlated with increased luciferase reactivation (*38*). Structurally, the interior of the $_{PARL}$Skd3 dodecamer provides a cavity sufficient to fit a folded or partially folded protein of ~70 kDa while also shielding the protein from aggregation and other off-pathway interactions (Fig. 3). The stable association of Skd3 oligomer with solubilized luciferase, some of which attained a native or near-native conformation (Fig. 4E), is most consistent with newly extracted substrate protein being encapsulated in the internal cavity of the Skd3 dodecamer. The fenestrated nature of the $_{PARL}$Skd3 dodecamer structure allows the facile exchange of water, small molecules, and cofactors, providing an environment in its internal cavity that is conducive to folding. On the other hand, the Skd3 dodecamer provides no obvious mechanism to initiate substrate translocation, as entry into the internal cavity through the pore ring would be in the opposite direction of force generation by protein-threading AAA$^+$ ATPases. We therefore suggest that the role of the Skd3 dodecamer occurs after substrate extraction by the hexamer, and

dodecamer assembly transitions Skd3 from the translocation/disaggregation phase to the refolding phase of its chaperone cycle (Fig. 7, step 3).

How newly extracted substrates enter the internal cavity of the dodecamer is unclear. The simplest model would involve a slippage of the substrate during translocation, leading to its release from the pore ring. Such a scenario could be favored by several factors: (i) limited pulling force from a single Skd3 AAA^+ ring, which may be insufficient to propel the complete threading of a large substrate such as luciferase; (ii) initiation of client folding, which would impede continued threading [ClpB releases partially translocated substrates upon encountering a folded domain in the substrate (*15*, *49*)]; and (iii) interaction of parts of the substrate protein with a second Skd3 hexamer, which would oppose continued threading. Regardless of the precise mechanism, release of partially threaded substrates has been observed with ClpB and was proposed to support substrate reactivation, by avoiding unnecessary unfolding of parts of the protein and preventing additional unfolded polypeptide segments from interfering with refolding (*15*, *49*).

Unique to Skd3 is the fusion of its AAA^+ ATPase moiety to the ARD, which remains the least understood component of this chaperone. Although the ARD is not structurally well resolved, our results here suggest multiple roles for this domain. First, the ARD mediates assembly of the Skd3 dodecamer. Second, the ARD could directly participate in substrate interactions (Fig. 6). Docking of the AlphaFold-predicted model in the dodecamer EM density further suggests that in the interior of the cavity, conserved hydrophobic and aromatic residues cluster on a concave surface in the helical domain of the Skd3 ARD and are shielded by the insertion domain (Fig. 6A). The deleterious effect of mutations at this surface on luciferase refolding and Aβ aggregation suppression by Skd3 (Fig. 6B and fig. S12) supports the role of this surface in chaperone-client interactions. It could be envisioned that the insertion domain acts as a flap that closes upon the hydrophobic cluster, and its opening would expose an extensive hydrophobic groove that mediate interaction with hydrophobic residues on unfolded and partially folded substrate proteins. These observations, together with consideration of the direction of substrate threading by the Skd3 hexamer, further place the ARDs as the initial sites of contact with the protein aggregate (Fig. 7, step 1).

We suggest the following working model for the chaperone cycle of $_{PARL}$Skd3 (Fig. 7). Hexameric $_{PARL}$Skd3 mediates the recognition of protein aggregates via its ARD and initiates ATP-driven threading of the substrate polypeptide through its pore ring (step 1). For client proteins such as luciferase, partial threading is sufficient to dislodge Skd3-bound substrates from the aggregate, freeing the ARDs to initiate dodecamer assembly (step 2). Solubilized but unfolded client proteins are captured in the internal cavity of the dodecamer, which provides an aqueous and confined environment in which substrate proteins can sample the folding trajectory while being protected from aggregation (step 3). It appears that client proteins such as luciferase can attain either the native or near-native conformation while associated with Skd3. As the dodecamer interface is dynamic, its disassembly provides a mechanism to release the substrate protein (step 4). Many aspects of this model remain to be tested and understood, including the molecular determinants that regulate Skd3 assembly, the degree of substrate threading required for solubilization, whether and how the Skd3 dodecamer senses and regulates client conformation, and whether additional functions are associated with the higher-order assembly state of Skd3.

The mitochondrial IMS is a crowded and complex environment with diverse and challenging proteostatic demands. Besides a small number of specialized chaperones, no additional general chaperones besides Skd3 have been identified in this space. The multiple chaperone activities of Skd3 may be particularly suited to the diverse proteostatic needs in this environment. On the other hand, the dimension of the Skd3 dodecamer cavity imposes a size limit on IMS proteins that can be refolded by this chaperone. It remains to be understood which one of its chaperone activities described here plays the dominant role in vivo, and how Skd3 cooperates with the other chaperones and proteases to maintain proper protein folding and quality control in this space.

MATERIALS AND METHODS

Plasmids

Codon-optimized DNA fragments encoding $_{PARL}$Skd3 and $_{MPP}$Skd3 (Twist Biosciences) were cloned into the pET28-His_6-SUMO plasmid behind the SUMO moiety using Gibson assembly. To increase the efficiency of SUMO protease cleavage, a GGS linker sequence was introduced at the N terminus of $_{MPP}$Skd3 coding sequence. Site-directed mutagenesis of $_{PARL}$Skd3 and $_{MPP}$Skd3 was carried out using the QuikChange mutagenesis protocol (Agilent). To express $_{PARL}$Skd3_ARD, a stop codon was introduced after R327 using the QuikChange mutagenesis protocol.

The coding sequence for *Photinus pyralis* luciferase was cloned between the Nco I and Xho I sites in pET28 to generate pET28-Luciferase-His_6. pHis_6-SUMO-Ssa1 and pUlp1-His_6 for expression of Ssa1 and Ulp1 (SUMO protease), respectively, were gifts from E. Deuerling. Expression plasmids for Ydj1 and Sis1 were described in (*51*). pTrc-GroEL-D87K was a gift from E. Chapman. pPROEX-Htb-Hsp104 (#1230), pSG25-β-Gal (#63867), and pET-Sac-Abeta(M1-42) (#71875) were from Addgene.

Protein purification

BL21-DE3 cells harboring pET28-His_6-luciferase were grown to mid-log phase, and expression of luciferase was induced at 20°C for 18 hours with 0.5 mM isopropyl-β-D-thiogalactopyranoside (IPTG). Harvested cells were resuspended in luciferase buffer [10 mM Na_2HPO_4 (pH 7.4), 10 mM NaH_2PO_4, and 500 mM NaCl] containing lysozyme (0.5 mg/ml) and 20 mM imidazole, incubated on ice for 30 min, and lysed using sonication. Clarified lysate was loaded on Ni-HP Sepharose (GE), washed with 20 column volume (CV) luciferase buffer containing 20 mM imidazole, and eluted with luciferase buffer containing 500 mM imidazole. Eluted fractions were dialyzed in anion exchange buffer [50 mM NaCl, 2 mM EDTA, 1 mM dithiothreitol (DTT), and 50 mM Tris-HCl buffer (pH 7.8)] and further purified using MonoQ 10/100 GL (GE Healthcare).

His_6-SUMO-$_{PARL}$Skd3, His_6-SUMO-$_{MPP}$Skd3, and their variants were expressed in BL21-CodonPlus-RIL cells (Agilent) grown to OD_{600} (optical density at 600 nm) of 0.6 to 0.8. Protein expression was induced at 16°C with 0.5 mM IPTG overnight. Cells from 1 liter of culture were resuspended in 15 ml of lysis buffer [40 mM K-Hepes (pH 7.5), 500 mM KCl, 20% glycerol, 5 mM ATP, 10 mM $MgCl_2$, 2 mM beta-mercaptoethanol (BME), 5 μM pepstatin A, and 1× protease inhibitor cocktail] supplemented with lysozyme

(1.5 mg/ml), incubated for 30 min at 4°C, and sonicated. Three milliliters of Ni-HP Sepharose (GE) preequilibrated in Ni-wash buffer [40 mM K-Hepes (pH 7.5), 500 mM KCl, 20% glycerol, 5 mM ATP, 10 mM $MgCl_2$, 2 mM BME, 2.5 μM pepstatin A, 0.2× protease inhibitor cocktail, and 50 mM imidazole] was mixed with clarified lysate and incubated for 1 hour and washed six times with 8 ml of Ni-wash buffer, three times with 3 ml of Ni-wash buffer supplemented with 20 mM ATP, and six more times with Ni-wash buffer. Fusion proteins were eluted using 12 ml of Ni-elution buffer [50 mM tris (pH 8.0), 500 mM KCl, 10% glycerol, 5 mM ATP, 10 mM $MgCl_2$, 2 mM BME, and 500 mM imidazole] and incubated with 1:100 molar ratio of purified Ulp1 for 2 hours. The mixture was concentrated in Amicon centrifugal filters (Millipore; molecular weight cutoff, 50 kDa) to ≤5 ml and purified over a Superdex 200 column (GE) in SK500 buffer [50 mM tris-HCl (pH 8.0), 500 mM KCl, 10% glycerol, 1 mM ATP, 10 mM $MgCl_2$, and 1 mM DTT]. Peak fractions were concentrated to 50 to 100 μM, supplemented with ATP to 5 mM, glycerol to 20%, and stored at −80°C.

Aβ42 was expressed and purified as described in (*52*). Ssa1, Ydj1, Sis1, Hsp104, and GroEL-D87K were purified as described (*51*, *53*, *54*). β-Gal was purified following the same protocol as that for GroEL-D87K.

Mass photometry

One hundred microliters of $_{PARL}$Skd3 was centrifuged at 18,000*g*, 30 min at 4°C, exchanged to K100 buffer [50 mM tris-HCl (pH 8.0), 100 mM KCl, 10 mM $MgCl_2$, and 1 mM DTT] containing 5 mM of the desired nucleotide over a PD SpinTrap G25 column (Cytiva), and diluted with the same buffer to submicromolar concentrations during measurements. Measurements were carried out on a Refeyen One^{MP} mass photometer (Refeyn Ltd.) with a 60-s acquisition time. Movies were analyzed using DiscoverMP (Refeyn Ltd.), and the contrast-to-mass conversion was achieved by calibration using the molecular weight standards bovine serum albumin (66 and 132 kDa), Sgt2 (80 kDa), thyroglobulin (330 kDa), and apoferritin (440 kDa). The events recorded from two to three independent measurements were pooled and fitted to Gaussian distributions to extract the mean molecular mass and relative amount of each peak.

Biochemical assays

Coupled luciferase disaggregation and refolding

Luciferase aggregates were prepared using two protocols. First, 50 μM purified luciferase was denatured in freshly prepared 8 M urea in refolding buffer [25 mM K-Hepes (pH 8.0), 150 mM KOAc, 10 mM $Mg(OAc)_2$, and 10 mM DTT] for 30 min at 30°C. Denatured luciferase was diluted 100-fold in refolding buffer and allowed to aggregate by incubation at room temperature for 5 min ($U_8L_{0.5}$). Second, 20 μM purified luciferase was denatured in 4 M urea in refolding buffer for 30 min at 30°C, diluted 100-fold in refolding buffer, and incubated at 30°C for 5 min before the addition of chaperones ($U_4L_{0.2}$).

Skd3 samples were centrifuged at 18,000*g* for 30 min at 4°C before all experiments. Coupled disaggregation-refolding reactions were initiated by mixing 50 nM $U_8L_{0.5}$ luciferase aggregates or 200 nM $U_4L_{0.2}$ luciferase aggregates with a solution containing 1 μM Skd3 or Hsp104/40/70 in refolding buffer supplemented with 5 mM ATP and ARS (consisting of 1 mM creatine phosphate and 0.25 μM creatine kinase). Reactions were incubated at 30°C. At indicated times, an aliquot was removed and diluted 20-fold in luciferase assay reagent (Promega), and chemiluminescence was measured in SpectraMax iD5 (Molecular Devices) using an integration time of 1 s. The percentage of refolded luciferase was calculated using a control reaction containing 50 nM native luciferase in refolding buffer, 5 mM ATP, and ARS. For reactions including the GroEL trap, purified GroEL-D87K was added either during or 5 min after initiation of the refolding reaction.

To measure the refolding of denatured luciferase (spontaneous or Skd3-assisted), 10 μM purified luciferase was denatured with 5 M GdmHCl for 1 hour at 25°C and diluted 100-fold into refolding buffer at 25°C containing 5 mM ATP and ARS, with or without $_{PARL}$Skd3 and GroEL-D87K. Chemiluminescence was measured at specified times, as described above.

Gel filtration chromatography

To evaluate the association of Skd3 with luciferase during the refolding reaction, reactions were carried out using $U_8L_{0.5}$ luciferase aggregates and were centrifuged (14,000 rpm, 10 min, 4°C) for 15 min after the initiation of the reaction. The supernatant was fractionated on Superdex 200 preequilibrated in refolding buffer containing 5 mM ATP. Fractions (0.5 ml) were collected and, after the void volume, immediately measured for luciferase activity. The individual fractions were further subjected to Western blot analysis using anti-His (luciferase) and anti-clpB (15743-1-AP, Proteintech) antibodies.

Luciferase disaggregation

Coupled disaggregation-refolding reaction was initiated as described above using $U_8L_{0.5}$ luciferase aggregates. At specified times, aliquots of the reaction were removed, mixed with apyrase (2 U/ml), and flash-frozen. Quenched reaction aliquots were centrifuged at 18,000*g* for 10 min at 4°C. Luciferase in the soluble and total samples was detected by Western blot using anti-His antibody. His_6-tagged cpSRP43 (10 nM), a 38-kDa plant chaperone, was mixed with the reaction after apyrase addition and used as a loading control.

ATPase assays

Assays were carried out at 25°C in refolding buffer. Skd3 samples were centrifuged at 18,000*g* for 30 min at 4°C before the measurements. Reactions were initiated by mixing indicated concentrations of Skd3 in refolding buffer containing 500 μM ATP with trace γ-^{32}P-ATP. Aliquots of the reaction were quenched in 0.75 M potassium phosphate (pH 3.3). γ-^{32}P-ATP and $^{32}P_i$ were separated by thin-layer chromatography and quantified by autoradiography. Observed ATPase rate constants ($V/[E]$) were plotted as a function of Skd3 concentration and fit to Eq. 1

$$\frac{V}{[E]} = \frac{k_{max}[\text{Skd3}]^n}{[\text{Skd3}]^n + {K_M}^n} \quad (1)$$

in which k_{max} is the ATPase rate constant at saturating Skd3 concentrations, K_M is the effective concentration for the formation of the ATPase-active complex, and n is the Hill coefficient.

Aβ42 fibrillation

Freshly purified monomeric Aβ42 (5 μM) was diluted in assay buffer [20 mM NaPI (pH 8.0) and 200 μM EDTA] with or without Skd3 and its variants at specified concentrations. All samples were prepared in low-binding Eppendorf tubes (Axygen) on ice by careful pipetting to avoid air bubbles. Each sample was then pipetted into multiple wells (100 μl per well) of a 96-well

half-area plate of black polystyrene with a clear bottom and polyethylene glycol (PEG) coating (Corning 3881). Plates were sealed with microseal (Bio-Rad, MSB1001) and incubated at 37°C under quiescent conditions in a plate reader (SpectraMax iD5). Amyloid formation was measured on the basis of the fluorescence of 6 μM thioflavin T at 482 nm. Data were fit using the AmyloFit software (*55*) to extract the halftimes of aggregation. For TEM imaging, a sample was collected when the aggregation reached the plateau value, diluted fivefold, and imaged by TEM. Five microliters of the reaction mixture was loaded on glow-discharged carbon-coated Cu grids (300 mesh, Ted Pella Inc.) for 1 min. Grids were washed twice in doubly deionized water and stained with 2% uranyl acetate for 1 min. Images from different areas of the grid were acquired using a 120-kV electron microscope (FEI Tecnai T12), and representative images are shown.

FITC-casein binding

Lyophilized FITC-casein (Sigma-Aldrich) was resuspended in water at 20 mg/ml and frozen at −80°C until use. Skd3 variants were exchanged into K100 buffer using G-25 columns (Cytiva). Buffers were supplemented with either no nucleotide, 1 mM ATPγS, or 5 mM ATP plus ARS. All measurements were carried out in the corresponding buffer at 25°C. Binding of casein to Skd3 was measured by changes in fluorescence anisotropy on FluoroLog 3-22 (Yobin Yvon), using 200 nM FITC-casein and serial additions of Skd3 to the indicated concentrations. The samples were excited at 482 nm, and the fluorescence anisotropy was recorded at 520 nm. To obtain the equilibrium dissociation constant between casein and Skd3, the data were fit to Eq. 2

$$A_{obs} = A_0 + \Delta A \frac{\left([casein] + [Skd3] + K_d - \sqrt{\{[casein] + [Skd3] + K_d\}^2 - \{4 \cdot [casein][Skd3]\}}\right)}{2 \cdot [casein]} \quad (2)$$

in which A_{obs} is the observed anisotropy value, A_0 is the anisotropy value of FITC-casein alone, ΔA is the change in anisotropy at saturating Skd3 concentrations relative to A_0, and K_d is the equilibrium dissociation constant for the interaction between FITC-casein and Skd3.

Cryo-EM

Data acquisition

For negative staining, 2.5 μl of the purified Skd3 (0.1 mg/ml) was applied to glow-discharged EM grids covered by a thin layer of continuous carbon film (TED Pella Inc.) and stained with 0.75% (w/v) uranyl formate solution. EM grids were imaged on a Tecnai T12 microscope (Thermo Fisher Scientific) operated at 120 kV with Gatan Rio Camera. Images were recorded at a magnification of ×52,000, resulting in a 2.2-Å pixel size on the specimen. Defocus was set to −1.5 to −2 μm.

For cryo-EM, 5 to 6 μl of purified $_{PARL}$Skd3_WB (1.06 mg/ml) were applied to glow-discharged holy carbon grids (Quantifoil 300 mesh Au R1.2/1.3). Four microliters of $_{PARL}$Skd3_WB (0.25 mg/ml) was applied onto holy carbon grids (Quantifoil 300 mesh Au R1.2/1.3) coated with PEG-amino–functionalized graphene oxide. The grids were blotted by Whatman no. 1 filter paper and plunge-frozen in liquid ethane using Mark IV Vitrobot (Thermo Fisher Scientific) with blotting times of 3 to 6 s at room temperature and over 90% humidity.

Cryo-EM datasets were collected at Stanford-SLAC Cryo-EM Center using EPU2.9 in Titan Krios G3i equipped with energy filter Selectris and Falcon4. From Quantifoil grids, 10,723 micrographs of no tilt data and 2151 micrographs of the tilt data were pooled to form dataset 1. From the PEG-amino grids (*56*), 10,854 micrographs were collected without tilt in dataset 2.

Cryo-EM data analysis

Micrograph CTF correction, particle picking and extraction, and three rounds of 2D classification were performed in CryoSPARC, resulting in 1.04 million particles from dataset 1 and 740,000 particles from dataset 2. For particles from each dataset, multiple rounds of ab initio reconstruction followed by heterogeneous refinement were performed in CryoSPARC. A total of 1.46 million remaining particles from both datasets were pooled and used for nonuniform (NU) refinement (fig. S2). The resolution of the high-resolution hexamer map was estimated using the gold standard Fourier shell correlation (FSC) = 0.143 criterion (*57*) and was 3.1 and 2.76 Å, respectively, for the unmasked and corrected tight masked FSC curves from CryoSPARC (fig. S3C and Table 1).

The unmasked half maps from the NU refinement were used for postprocessing by DeepEMhancer (*58*) using the highRes deep learning model and default training data provided by the DeepEMhancer authors. No further map sharpening was applied. The DeepEMhancer-generated map was used for model building in Coot and Phenix.

3DVA was carried out in CryoSPARC on downsampled particles from dataset 1 using five components. The first eigenvector showed large variability at the P1/P6 seam. Particles along this coordinate were displayed in 20 bins, and models generated from NU refinement of particles in the first three and last three bins were used as reference maps for heterogeneous refinement of all the purified particles from dataset 1. The particles in the extended and closed conformation generated in this procedure were used for NU refinement in CryoSPARC (fig. S2). The resolutions of both maps were estimated using the FSC = 0.143 criterion (*57*). Resolutions for the unmasked FSC curves from CryoSPARC were 3.5 and 3.3 Å, respectively, for the closed and open conformations; resolutions for corrected tight masked FSC curves from CryoSPARC were 3.1 and 2.9 Å, respectively, for the closed and open conformations (fig. S6, A and B, and Table 1).

Weak EM density was observed above the hexamer in the EM map generated by CryoSPARC, and 3D classification of a subset of these particles indicated that <20% are dodecamers. To better isolate dodecamer particles, the 1.78 million particles after 2D classification in CryoSPARC were imported into RELION (fig. S2). 3D classification with five classes was carried out to separate dodecamer and hexamer particles. A total of 521,000 dodecamer particles were selected for 3D refinement in RELION to generate the final dodecamer map (fig. S2). The resolution of the dodecamer was estimated to be 6.5 Å using unmasked FSC curves in RELION with FSC = 0.143 (fig. S7C). Masks were then generated for the lower or upper NBD and used for particle subtraction followed by 3D refinement (fig. S2). The resolutions of the maps from focused 3D refinement were 3.8 and 7.7 Å for the lower and upper NBD ring, respectively, as estimated using unmasked FSC curves with FSC = 0.143 in RELION.

Directional FSC curves for the hexamer and dodecamer maps were calculated using unmasked half maps as described in (*59*). Local resolution for each map was calculated in CryoSPARC and

visualized in Chimera. Star and bild files from CryoSPARC particles were generated using UCSF pyem. Map-model FSC was calculated in Phenix with the DeepEMhancer-processed hexamer map using an FSC threshold of 0.5.

Model building

An initial model of Skd3 was obtained using AlphaFold (*41*), and the NBD (residues 318 to 696) was docked into the P4 protomer of the high-resolution sharpened map of the hexamer using "dock and rebuild" in Phenix(*43*). Initial model building of the P4 protomer was built using Coot (*42*) and real space–refined with Phenix. This protomer was duplicated to fit the density of the remaining five protomers by rigid-body fitting, resulting in a hexameric model for the NBD ring that excludes two solvent-exposed loops (524 to 536 and 655 to 675). Iterative cycles of manual adjustments to this model were performed in Coot, followed by real-space refinements in Phenix. ATPγS was modeled into each protomer, including P1, which only had partial occupancy for the nucleotide. Chains A through F correspond to protomers P1 to P6, and chain P corresponds to the peptide substrate, which was modeled as a 14-residue poly-alanine chain.

Supplementary Materials

This PDF file includes:
Figs. S1 to S12
Legend for movie S1

Other Supplementary Material for this manuscript includes the following:
Movie S1

View/request a protocol for this paper from *Bio-protocol*.

REFERENCES AND NOTES

1. Y. E. Kim, M. S. Hipp, A. Bracher, M. Hayer-Hartl, F. U. Hartl, Molecular chaperone functions in protein folding and proteostasis. *Annu. Rev. Biochem.* **82**, 323–355 (2013).
2. F. U. Hartl, Protein misfolding diseases. *Annu. Rev. Biochem.* **86**, 21–26 (2017).
3. R. Rosenzweig, N. B. Nillegoda, M. P. Mayer, B. Bukau, The Hsp70 chaperone network. *Nat. Rev. Mol. Cell Biol.* **20**, 665–680 (2019).
4. H. H. Kampinga, E. A. Craig, The HSP70 chaperone machinery: J proteins as drivers of functional specificity. *Nat. Rev. Mol. Cell Biol.* **11**, 579–592 (2010).
5. H. Rampelt, M. P. Mayer, B. Bukau, Nucleotide exchange factors for Hsp70 chaperones. *Methods Mol. Biol.* **1709**, 179–188 (2018).
6. R. Imamoglu, D. Balchin, M. Hayer-Hartl, F. U. Hartl, Bacterial Hsp70 resolves misfolded states and accelerates productive folding of a multi-domain protein. *Nat. Commun.* **11**, 365 (2020).
7. S. K. Sharma, P. De los Rios, P. Christen, A. Lustig, P. Goloubinoff, The kinetic parameters and energy cost of the Hsp70 chaperone as a polypeptide unfoldase. *Nat. Chem. Biol.* **6**, 914–920 (2010).
8. M. Hayer-Hartl, A. Bracher, F. U. Hartl, The GroEL-GroES chaperonin machine: A nano-cage for protein folding. *Trends Biochem. Sci.* **41**, 62–76 (2016).
9. H. R. Saibil, W. A. Fenton, D. K. Clare, A. L. Horwich, Structure and allostery of the chaperonin GroEL. *J. Mol. Biol.* **425**, 1476–1487 (2013).
10. D. Gestaut, S. H. Roh, B. Ma, G. Pintilie, L. A. Joachimiak, A. Leitner, T. Walzthoeni, R. Aebersold, W. Chiu, J. Frydman, The chaperonin TRiC/CCT associates with prefoldin through a conserved electrostatic interface essential for cellular proteostasis. *Cell* **177**, 751–765.e15 (2019).
11. S. Ungelenk, F. Moayed, C. T. Ho, T. Grousl, A. Scharf, A. Mashaghi, S. Tans, M. P. Mayer, A. Mogk, B. Bukau, Small heat shock proteins sequester misfolding proteins in near-native conformation for cellular protection and efficient refolding. *Nat. Commun.* **7**, 13673 (2016).
12. M. E. DeSantis, E. H. Leung, E. A. Sweeny, M. E. Jackrel, M. Cushman-Nick, A. Neuhaus-Follini, S. Vashist, M. A. Sochor, M. N. Knight, J. Shorter, Operational plasticity enables hsp104 to disaggregate diverse amyloid and nonamyloid clients. *Cell* **151**, 778–793 (2012).
13. J. R. Glover, S. Lindquist, Hsp104, Hsp70, and Hsp40: A novel chaperone system that rescues previously aggregated proteins. *Cell* **94**, 73–82 (1998).
14. C. Schlieker, J. Weibezahn, H. Patzelt, P. Tessarz, C. Strub, K. Zeth, A. Erbse, J. Schneider-Mergener, J. W. Chin, P. G. Schultz, B. Bukau, A. Mogk, Substrate recognition by the AAA+ chaperone ClpB. *Nat. Struct. Mol. Biol.* **11**, 607–615 (2004).
15. T. Haslberger, B. Bukau, A. Mogk, Towards a unifying mechanism for ClpB/Hsp104-mediated protein disaggregation and prion propagation. *Biochem. Cell Biol.* **88**, 63–75 (2010).
16. C. Schlieker, I. Tews, B. Bukau, A. Mogk, Solubilization of aggregated proteins by ClpB/DnaK relies on the continuous extraction of unfolded polypeptides. *FEBS Lett.* **578**, 351–356 (2004).
17. J. Weibezahn, P. Tessarz, C. Schlieker, R. Zahn, Z. Maglica, S. Lee, H. Zentgraf, E. U. Weber-Ban, D. A. Dougan, F. T. F. Tsai, A. Mogk, B. Bukau, Thermotolerance requires refolding of aggregated proteins by substrate translocation through the central pore of ClpB. *Cell* **119**, 653–665 (2004).
18. S. N. Gates, A. Martin, Stairway to translocation: AAA+ motor structures reveal the mechanisms of ATP-dependent substrate translocation. *Protein Sci.* **29**, 407–419 (2020).
19. S. N. Gates, A. L. Yokom, J. Lin, M. E. Jackrel, A. N. Rizo, N. M. Kendsersky, C. E. Buell, E. A. Sweeny, K. L. Mack, E. Chuang, M. P. Torrente, M. Su, J. Shorter, D. R. Southworth, Ratchet-like polypeptide translocation mechanism of the AAA+ disaggregase Hsp104. *Science* **357**, 273–279 (2017).
20. A. N. Rizo, J. Lin, S. N. Gates, E. Tse, S. M. Bart, L. M. Castellano, F. DiMaio, J. Shorter, D. R. Southworth, Structural basis for substrate gripping and translocation by the ClpB AAA+ disaggregase. *Nat. Commun.* **10**, 2393 (2019).
21. J. Shorter, S. Lindquist, Hsp104, Hsp70 and Hsp40 interplay regulates formation, growth and elimination of Sup35 prions. *EMBO J.* **27**, 2712–2724 (2008).
22. R. Rosenzweig, S. Moradi, A. Zarrine-Afsar, J. R. Glover, L. E. Kay, Unraveling the mechanism of protein disaggregation through a ClpB-DnaK interaction. *Science* **339**, 1080–1083 (2013).
23. F. Seyffer, E. Kummer, Y. Oguchi, J. Winkler, M. Kumar, R. Zahn, V. Sourjik, B. Bukau, A. Mogk, Hsp70 proteins bind Hsp100 regulatory M domains to activate AAA+ disaggregase at aggregate surfaces. *Nat. Struct. Mol. Biol.* **19**, 1347–1355 (2012).
24. A. J. Erives, J. S. Fassler, Metabolic and chaperone gene loss marks the origin of animals: Evidence for Hsp104 and Hsp78 chaperones sharing mitochondrial enzymes as clients. *PLOS ONE* **10**, e0117192 (2015).
25. Z. Spaulding, I. Thevarajan, L. G. Schrag, L. Zubcevic, A. Zolkiewska, M. Zolkiewski, Human mitochondrial AAA+ ATPase SKD3/CLPB assembles into nucleotide-stabilized dodecamers. *Biochem. Biophys. Res. Commun.* **602**, 21–26 (2022).
26. I. Thevarajan, M. Zolkiewski, A. Zolkiewska, Human CLPB forms ATP-dependent complexes in the mitochondrial intermembrane space. *Int. J. Biochem. Cell Biol.* **127**, 105841 (2020).
27. R. R. Cupo, J. Shorter, Skd3 (human ClpB) is a potent mitochondrial protein disaggregase that is inactivated by 3-methylglutaconic aciduria-linked mutations. *eLife* **9**, e55279 (2020).
28. D. Mroz, H. Wyszkowski, T. Szablewski, K. Zawieracz, R. Dutkiewicz, K. Bury, S. B. Wortmann, R. A. Wevers, S. Zietkiewicz, CLPB (caseinolytic peptidase B homolog), the first mitochondrial protein refoldase associated with human disease. *Biochim. Biophys. Acta Gen. Subj.* **1864**, 129512 (2020).
29. T. Yoshinaka, H. Kosako, T. Yoshizumi, R. Furukawa, Y. Hirano, O. Kuge, T. Tamada, T. Koshiba, Structural basis of mitochondrial scaffolds by prohibitin complexes: Insight into a role of the coiled-coil region. *iScience* **19**, 1065–1078 (2019).
30. S. B. Wortmann, S. Zietkiewicz, M. Kousi, R. Szklarczyk, T. B. Haack, S. W. Gersting, A. C. Muntau, A. Rakovic, G. H. Renkema, R. J. Rodenburg, T. M. Strom, T. Meitinger, M. E. Rubio-Gozalbo, E. Chrusciel, F. Distelmaier, C. Golzio, J. H. Jansen, C. van Karnebeek, Y. Lillquist, T. Lucke, K. Ounap, R. Zordania, J. Yaplito-Lee, H. van Bokhoven, J. N. Spelbrink, F. M. Vaz, M. Pras-Raves, R. Ploski, E. Pronicka, C. Klein, M. A. Willemsen, A. P. de Brouwer, H. Prokisch, N. Katsanis, R. A. Wevers, CLPB mutations cause 3-methylglutaconic aciduria, progressive brain atrophy, intellectual disability, congenital neutropenia, cataracts, movement disorder. *Am. J. Hum. Genet.* **96**, 245–257 (2015).
31. J. M. Capo-Chichi, S. Boissel, E. Brustein, S. Pickles, C. Fallet-Bianco, C. Nassif, L. Patry, S. Dobrzeniecka, M. Liao, D. Labuda, M. E. Samuels, F. F. Hamdan, C. Vande Velde, G. A. Rouleau, P. Drapeau, J. L. Michaud, Disruption of *CLPB* is associated with congenital microcephaly, severe encephalopathy and 3-methylglutaconic aciduria. *J. Med. Genet.* **52**, 303–311 (2015).
32. M. Kanabus, R. Shahni, J. W. Saldanha, E. Murphy, V. Plagnol, W. V. Hoff, S. Heales, S. Rahman, Bi-allelic CLPB mutations cause cataract, renal cysts, nephrocalcinosis and 3-methylglutaconic aciduria, a novel disorder of mitochondrial protein disaggregation. *J. Inherit. Metab. Dis.* **38**, 211–219 (2015).
33. A. Kiykim, W. Garncarz, E. Karakoc-Aydiner, A. Ozen, E. Kiykim, G. Yesil, K. Boztug, S. Baris, Novel CLPB mutation in a patient with 3-methylglutaconic aciduria causing severe neurological involvement and congenital neutropenia. *Clin. Immunol.* **165**, 1–3 (2016).

34. S. B. Wortmann, R. A. Wevers, CLPB deficiency, in *GeneReviews((R))*, M. P. Adam, H. H. Ardinger, R. A. Pagon, S. E. Wallace, L. J. H. Bean, K. W. Gripp, G. M. Mirzaa, A. Amemiya, Eds. (University of Washington, Seattle, 1993).
35. S. B. Wortmann, S. Zietkiewicz, S. Guerrero-Castillo, R. G. Feichtinger, M. Wagner, J. Russell, C. Ellaway, D. Mroz, H. Wyszkowski, D. Weis, I. Hannibal, C. von Stulpnagel, A. Cabrera-Orefice, U. Lichter-Konecki, J. Gaesser, R. Windreich, K. C. Myers, R. Lorsbach, R. C. Dale, S. Gersting, C. E. Prada, J. Christodoulou, N. I. Wolf, H. Venselaar, J. A. Mayr, R. A. Wevers, Neutropenia and intellectual disability are hallmarks of biallelic and de novo CLPB deficiency. *Genet. Med.* **23**, 1705–1714 (2021).
36. R. Edwards, S. Gerlich, K. Tokatlidis, The biogenesis of mitochondrial intermembrane space proteins. *Biol. Chem.* **401**, 737–747 (2020).
37. J. M. Herrmann, J. Riemer, Oxidation and reduction of cysteines in the intermembrane space of mitochondria: Multiple facets of redox control. *Antioxid. Redox Signal.* **13**, 1323–1326 (2010).
38. R. R. Cupo, A. N. Rizo, G. A. Braun, E. Tse, E. Chuang, K. Gupta, D. R. Southworth, J. Shorter, Unique structural features govern the activity of a human mitochondrial AAA+ disaggregase, Skd3. *Cell Rep.* **40**, 111408 (2022).
39. D. Wu, Y. Liu, Y. Dai, G. Wang, G. Lu, Y. Chen, N. Li, J. Lin, N. Gao, Comprehensive structural characterization of the human AAA+ disaggregase CLPB in the apo- and substrate-bound states reveals a unique mode of action driven by oligomerization. *PLOS Biol.* **21**, e3001987 (2023).
40. G. Young, N. Hundt, D. Cole, A. Fineberg, J. Andrecka, A. Tyler, A. Olerinyova, A. Ansari, E. G. Marklund, M. P. Collier, S. A. Chandler, O. Tkachenko, J. Allen, M. Crispin, N. Billington, Y. Takagi, J. R. Sellers, C. Eichmann, P. Selenko, L. Frey, R. Riek, M. R. Galpin, W. B. Struwe, J. L. P. Benesch, P. Kukura, Quantitative mass imaging of single biological macromolecules. *Science* **360**, 423–427 (2018).
41. J. Jumper, R. Evans, A. Pritzel, T. Green, M. Figurnov, O. Ronneberger, K. Tunyasuvunakool, R. Bates, A. Zidek, A. Potapenko, A. Bridgland, C. Meyer, S. A. A. Kohl, A. J. Ballard, A. Cowie, B. Romera-Paredes, S. Nikolov, R. Jain, J. Adler, T. Back, S. Petersen, D. Reiman, E. Clancy, M. Zielinski, M. Steinegger, M. Pacholska, T. Berghammer, S. Bodenstein, D. Silver, O. Vinyals, A. W. Senior, K. Kavukcuoglu, P. Kohli, D. Hassabis, Highly accurate protein structure prediction with AlphaFold. *Nature* **596**, 583–589 (2021).
42. P. Emsley, K. Cowtan, Coot: Model-building tools for molecular graphics. *Acta Crystallogr. D Biol. Crystallogr.* **60**, 2126–2132 (2004).
43. P. D. Adams, P. V. Afonine, G. Bunkoczi, V. B. Chen, I. W. Davis, N. Echols, J. J. Headd, L. W. Hung, G. J. Kapral, R. W. Grosse-Kunstleve, A. J. McCoy, N. W. Moriarty, R. Oeffner, R. J. Read, D. C. Richardson, J. S. Richardson, T. C. Terwilliger, P. H. Zwart, PHENIX: A comprehensive Python-based system for macromolecular structure solution. *Acta Crystallogr. D Biol. Crystallogr.* **66**, 213–221 (2010).
44. P. Forrer, H. K. Binz, M. T. Stumpp, A. Pluckthun, Consensus design of repeat proteins. *Chembiochem* **5**, 183–189 (2004).
45. J. S. Weissman, Y. Kashi, W. A. Fenton, A. L. Horwich, GroEL-mediated protein folding proceeds by multiple rounds of binding and release of nonnative forms. *Cell* **78**, 693–702 (1994).
46. M. E. Jackrel, M. E. DeSantis, B. A. Martinez, L. M. Castellano, R. M. Stewart, K. A. Caldwell, G. A. Caldwell, J. Shorter, Potentiated Hsp104 variants antagonize diverse proteotoxic misfolding events. *Cell* **156**, 170–182 (2014).
47. S. Lee, B. Sielaff, J. Lee, F. T. Tsai, CryoEM structure of Hsp104 and its mechanistic implication for protein disaggregation. *Proc. Natl. Acad. Sci. U.S.A.* **107**, 8135–8140 (2010).
48. J. Shorter, D. R. Southworth, Spiraling in control: Structures and mechanisms of the Hsp104 disaggregase. *Cold Spring Harb. Perspect. Biol.* **11**, a034033 (2019).
49. T. Haslberger, A. Zdanowicz, I. Brand, J. Kirstein, K. Turgay, A. Mogk, B. Bukau, Protein disaggregation by the AAA+ chaperone ClpB involves partial threading of looped polypeptide segments. *Nat. Struct. Mol. Biol.* **15**, 641–650 (2008).
50. H. Yoo, J. A. M. Bard, E. V. Pilipenko, D. A. Drummond, Chaperones directly and efficiently disperse stress-triggered biomolecular condensates. *Mol. Cell* **82**, 741–755.e11 (2022).
51. H. Cho, W. J. Shim, Y. Liu, S. O. Shan, J-domain proteins promote client relay from Hsp70 during tail-anchored membrane protein targeting. *J. Biol. Chem.* **296**, 100546 (2021).
52. D. M. Walsh, E. Thulin, A. M. Minogue, N. Gustavsson, E. Pang, D. B. Teplow, S. Linse, A facile method for expression and purification of the Alzheimer's disease-associated amyloid beta-peptide. *FEBS J.* **276**, 1266–1281 (2009).
53. E. A. Sweeny, M. E. DeSantis, J. Shorter, Purification of hsp104, a protein disaggregase.*J. Vis. Exp.*, e3190 (2011).
54. J. Buchner, M. Schmidt, M. Fuchs, R. Jaenicke, R. Rudolph, F. X. Schmid, T. Kiefhaber, GroE facilitates refolding of citrate synthase by suppressing aggregation. *Biochemistry* **30**, 1586–1591 (1991).
55. G. Meisl, J. B. Kirkegaard, P. Arosio, T. C. Michaels, M. Vendruscolo, C. M. Dobson, S. Linse, T. P. Knowles, Molecular mechanisms of protein aggregation from global fitting of kinetic models. *Nat. Protoc.* **11**, 252–272 (2016).
56. F. Wang, Z. Yu, M. Betegon, M. G. Campbell, T. Aksel, J. Zhao, S. Li, S. M. Douglas, Y. Cheng, D. A. Agard, Amino and PEG-amino graphene oxide grids enrich and protect samples for high-resolution single particle cryo-electron microscopy. *J. Struct. Biol.* **209**, 107437 (2020).
57. P. B. Rosenthal, R. Henderson, Optimal determination of particle orientation, absolute hand, and contrast loss in single-particle electron cryomicroscopy. *J. Mol. Biol.* **333**, 721–745 (2003).
58. R. Sanchez-Garcia, J. Gomez-Blanco, A. Cuervo, J. M. Carazo, C. O. S. Sorzano, J. Vargas, DeepEMhancer: A deep learning solution for cryo-EM volume post-processing. *Commun. Biol.* **4**, 874 (2021).
59. S. Dang, S. Feng, J. Tien, C. J. Peters, D. Bulkley, M. Lolicato, J. Zhao, K. Zuberbuhler, W. Ye, L. Qi, T. Chen, C. S. Craik, Y. N. Jan, D. L. Minor Jr., Y. Cheng, L. Y. Jan, Cryo-EM structures of the TMEM16A calcium-activated chloride channel. *Nature* **552**, 426–429 (2017).
60. H. Ashkenazy, S. Abadi, E. Martz, O. Chay, I. Mayrose, T. Pupko, N. Ben-Tal, ConSurf 2016: An improved methodology to estimate and visualize evolutionary conservation in macromolecules. *Nucleic Acids Res.* **44**, W344–W350 (2016).

Acknowledgments: We thank H. Wu (UCSF) and S. Petrovic (CalTech) for assistance with cryo-EM data analysis and structural modeling, C. Wang for construction of the luciferase expression plasmid, E. Chapman for the pTrc-GroEL_D87K plasmid, E. Deuerling for plasmids pHis$_6$-SUMO-Ssa1 and pUlp1-His$_6$, and members of the Shan and Cheng groups for discussions and comments on the manuscript. **Funding:** S.-o.S. was supported by National Institutes of Health (NIH) grant R35 GM136321 and a travel fund from the Burroughs Welcome Foundation. U.S.C. was supported by NIH fellowship F32GM137463. Y.C. is supported by NIH grant R35GM140847 and is an Investigator of Howard Hughes Medical Institute. Cryo-EM data were collected at UCSF cryo-EM facility, supported by NIH grants S10OD021741 and 1S10OD026881, and the Stanford-SLAC Cryo-EM Center (S^{2}C^2), supported by the National Institutes of Health Common Fund Transformative High-Resolution Cryo-Electron Microscopy program (U24 GM129541). **Author contributions:** Conceptualization: S.-o.S. Methodology: U.S.C., Z.Y., and Y.C. Investigation: A.G., S.-o.S., A.S., A.M.L., and Z.Y. Visualization: A.M.L., A.S., and A.G. Supervision: S.-o.S., Z.Y., and U.S.C. Writing—original draft: S.-o.S., A.M.L., A.S., and A.G. Writing—review and editing: all authors. **Competing interests:** Y.C. is a member of scientific advisory board of ShuiMu BioSciences. The other authors declare that they have no competing interests. **Data and materials availability:** Cryo-EM maps and model coordinates are deposited in the EMDB and PDB as PDB entry ID 7US2 and EMDB entry ID EMD-26722 [high-resolution map of PARL-cleaved Skd3 (human ClpB) E455Q Nucleotide Binding Domain hexamer bound to ATPgammaS, open conformation]; EMD-26725 [3DVA derived map of PARL-cleaved Skd3 (human ClpB) E455Q Nucleotide Binding Domain hexamer bound to ATPgammaS, open conformation]; EMD-26726 [3DVA derived map of PARL-cleaved Skd3 (human ClpB) E455Q Nucleotide Binding Domain hexamer bound to ATPgammaS, closed conformation]; EMD-26728 [PARL-cleaved Skd3 (human ClpB) E455Q dodecamer bound to ATPgammaS]. All data needed to evaluate the conclusions in the paper are present in the paper and/or the Supplementary Materials. pSG25-β-Gal (#63867) and pET-Sac-Abeta(M1-42) (#71875) can be purchased from Addgene pending a completed material transfer agreement.

Submitted 27 October 2022
Accepted 4 April 2023
Published 10 May 2023
10.1126/sciadv.adf5336